



1 **Title**

2 Interpreting the cause of bound earthquakes at underground injection experiments

3  
4 **Authors**

5 Ryan Schultz<sup>1\*</sup>, Linus Villiger<sup>1</sup>, Valentin Gischig<sup>1</sup>, Stefan Wiemer<sup>1</sup>

6  
7 <sup>1</sup> Swiss Seismological Service, ETH Zürich, Zürich, Switzerland

8 \* corresponding author: [Ryan.Schultz@sed.ethz.ch](mailto:Ryan.Schultz@sed.ethz.ch)

9  
10 **Abstract**

11         Constraining the maximum possible magnitude ( $M_{\text{MAX}}$ ) of an induced earthquake  
12 sequence is a challenging process with important implications for managing risks. CAP-tests  
13 are a suite of statistical tests that can infer, quantify, and select best-fitting  $M_{\text{MAX}}$  models via  
14 an earthquake catalogue's magnitudes. We use CAP-tests to discern between bound/unbound  
15 earthquake sequences at underground laboratories, where high-resolution and near-field  
16 geophysical observations are abundant. There, we find clear evidence for bound sequences,  
17 where magnitude growth was restricted during stimulation. Furthermore, bound sequences  
18 tend to be associated with stimulations that occurred within intact rock. On the other hand,  
19 unbound sequences tended to be associated with stimulations where hydraulic fractures  
20 interacted with relatively large pre-existing faults/fractures. We further examine bound  
21 sequences by fitting magnitude growth to a generalized family of  $M_{\text{MAX}}$  functions. This  
22 process appears to be able to aggregate bound sequences into categories consistent with  
23 theoretical considerations (*e.g.*, tectonic, tensile-crack, or shear-crack). These results provide  
24 a basis for validating and interpreting bound sequences in controlled experiments, which is  
25 important for extrapolating to larger-scale observations. Overall, CAP-tests appear to be a  
26 promising avenue for constraining  $M_{\text{MAX}}$  from earthquake catalogue data.

27  
28 **Short Summary**

29         We use statistical tests to infer  $M_{\text{MAX}}$  from an earthquake catalogue and focus on data  
30 from three underground laboratories with controlled injection experiments. There, we find  
31 clear evidence for  $M_{\text{MAX}}$  bounds and corroborate interpretations of fracture growth against  
32 other geophysical studies. Unbound sequences occur when stimulation is directed towards pre-  
33 existing faults. The validation of our methods against well-studied cases is encouraging and  
34 will help validate future interpretations.

35  
36 **Key Points**



- 37      • Bound earthquake sequences (*i.e.*, physically restricted maximum magnitudes) were  
38              unambiguously identified in underground laboratories.
- 39      • Bound sequences tend to be associated with stimulation stages, while unbound  
40              sequences tend to inject into pre-existing faults/fractures.
- 41      • Maximum magnitudes aggregate into four categories that are consistent with  
42              theoretical expectations.
- 43
- 44



## 45 Main text

### 46 1. Introduction

47 Any process that has the potential to alter stresses in the subsurface also has the  
 48 potential to trigger earthquakes (Moein et al., 2023). To date, many types of anthropogenic  
 49 operations have induced earthquakes including wastewater disposal, hydraulic fracturing,  
 50 enhanced geothermal systems, geological carbon sequestration, reservoir impoundment, and  
 51 mining (Majer et al., 2007; Foulger et al., 2018; Schultz et al., 2020). In some cases, these  
 52 events have grown large enough to be felt, damaging, or even harmful (Atkinson et al., 2016;  
 53 Grigoli et al., 2018). In reaction to some of these cases, social concerns have resulted in  
 54 subsurface development moratoriums (Kettlety et al., 2021; Muntendam-Bos et al., 2022).

55 The need to manage the risks of induced earthquakes has been recognized (Bommer,  
 56 2022; Zhou et al., 2024). The *de facto* approach to risk management centralizes around the  
 57 traffic light protocol (Bommer et al., 2006), which delineates when an operation must stop (*i.e.*,  
 58 the red-light). Typically, red-lights are designed as magnitude thresholds (Schultz et al., 2021a;  
 59 2021b; 2023a). Despite the widespread adoption of traffic light protocols, relatively little is  
 60 understood about the growth of induced earthquake magnitudes. Some recent papers have  
 61 begun examining this topic; for example, by attempting to forecast the next largest event  
 62 (Mendecki, 2016; Cao et al., 2020; 2024; Schultz et al., 2023b; Verdon et al., 2023; 2024; Yin  
 63 et al., 2024). However, these approaches are unable to discern the adequacy of input models.  
 64 These topics are important for understanding trailing earthquakes (Schultz et al., 2022) and  
 65 magnitude jumps (Verdon & Bommer, 2021), which are among the most important factors for  
 66 designing risk-informed red-lights (Schultz et al., 2021a).

67 A common theme underlying these efforts is constraining the maximum possible  
 68 magnitude ( $M_{MAX}$ ), given its prominence for induced seismicity hazard quantification  
 69 (Bommer & Verdon, 2024). While there are numerous theoretical models that could possibly  
 70 limit  $M_{MAX}$  (McGarr, 2014; Hallo et al., 2014; Galis et al., 2017; Elsworth, et al., 2025; Im &  
 71 Avouac, 2025; Sáez et al., 2025), there are relatively few methods available to reliably validate  
 72 them with empirical data (Holschneider et al., 2014; Pisarenko & Rodkin, 2022). In fact,  
 73 empirically constraining  $M_{MAX}$  from a catalogue is known to be a challenging task that is  
 74 usually only possible in special circumstances (Holschneider et al., 2011; Zöller et al., 2016).  
 75 Given the conflict between needing  $M_{MAX}$  constraints against the lack of robust approaches,  
 76 expert solicitation is often used as a substitute (DeDontney et al., 2016). Thus, there is a need  
 77 to replace subjective/opinion-based methods with more quantitative measures for  $M_{MAX}$ .



78           Based on this need, CAP-tests were designed as a suite of statistical tests to infer and  
 79           quantify the presence of  $M_{MAX}$  within a catalogue of data. Specifically, this approach compares  
 80           the distribution of earthquake magnitudes ( $M$ ) against the distribution of jumps in the largest  
 81           magnitude events ( $\Delta M_{LRG}$ ): when they are the same distribution, the catalogue is unbound and  
 82           there is no  $M_{MAX}$  (and *vice versa*) (Schultz, 2024). Synthetic testing suggests that this problem  
 83           reformulation can be more sensitive to  $M_{MAX}$  than traditional approaches (Schultz, 2024).  
 84           CAP-tests are broken into three component parts: the KS-test as a hypothesis test to infer the  
 85           presence of  $M_{MAX}$ , the MLE-test to quantify the value of  $M_{MAX}$ , and the EW-test to select the  
 86           theoretical  $M_{MAX}$  model that explains the catalogue data best. We provide the full  
 87           methodological details of CAP-tests in Section 2.

88           The application of CAP-tests to relatively larger magnitude induced seismicity cases  
 89           found that these cases behaved in an unbound manner (Schultz, 2024) – suggesting that the use  
 90           of theoretical  $M_{MAX}$  models (McGarr, 2014; Hallo et al., 2014; Galis et al., 2017; Elsworth, et  
 91           al., 2025; Im & Avouac, 2025; Sáez et al., 2025) are not appropriate during these fault  
 92           reactivations. On the other hand, smaller-scale cases of induced seismicity (e.g., Utah FORGE,  
 93           Preston New Road, Helsinki St1) from hydraulic stimulation indicated strong evidence for  
 94           bound magnitude growth via an  $M_{MAX}$  (Schultz et al., 2025). Furthermore, some stimulation  
 95           stages transitioned from a bound process into an unbound one; this was interpreted as these  
 96           particular stages reactivating pre-existing faults instead of stimulating new fractures. That said,  
 97           subsurface unknowns/uncertainties hamper an unambiguous interpretation for these field-scale  
 98           cases.

99           To better address subsurface unknowns/uncertainties, several underground laboratories  
 100           (UGLs) have performed hydraulic fracturing experiments with varying scales/scopes. These  
 101           intermediate-scale experiments aim to fill a gap between laboratory studies and field-scale  
 102           observations: accessing near-field geophysical observations (that are infeasible at the field-  
 103           scale) in a semi-realistic *in situ* setting. Said another way, UGL data was collected with the  
 104           intention of delineating and interpreting fracture stimulation. Thus, the complementary data  
 105           from UGLs is ideal for better interpreting bound sequences (found via CAP-tests). This  
 106           comparison has the potential to elucidate an underlying mechanism for bound induced  
 107           seismicity sequences. This significant, since it starts to link statistical inferences of  $M_{MAX}$  to  
 108           physical processes.

109           In this study, we collect data from three UGLs: the Äspö Hard Rock Laboratory (Zang  
 110           et al., 2019; 2021), the Sanford Underground Research Facility (Dobson et al., 2018; Kneafsey  
 111           et al., 2018; Morris et al., 2018), and the Grimsel Test Site (Gischig et al., 2016; Amann et al.,

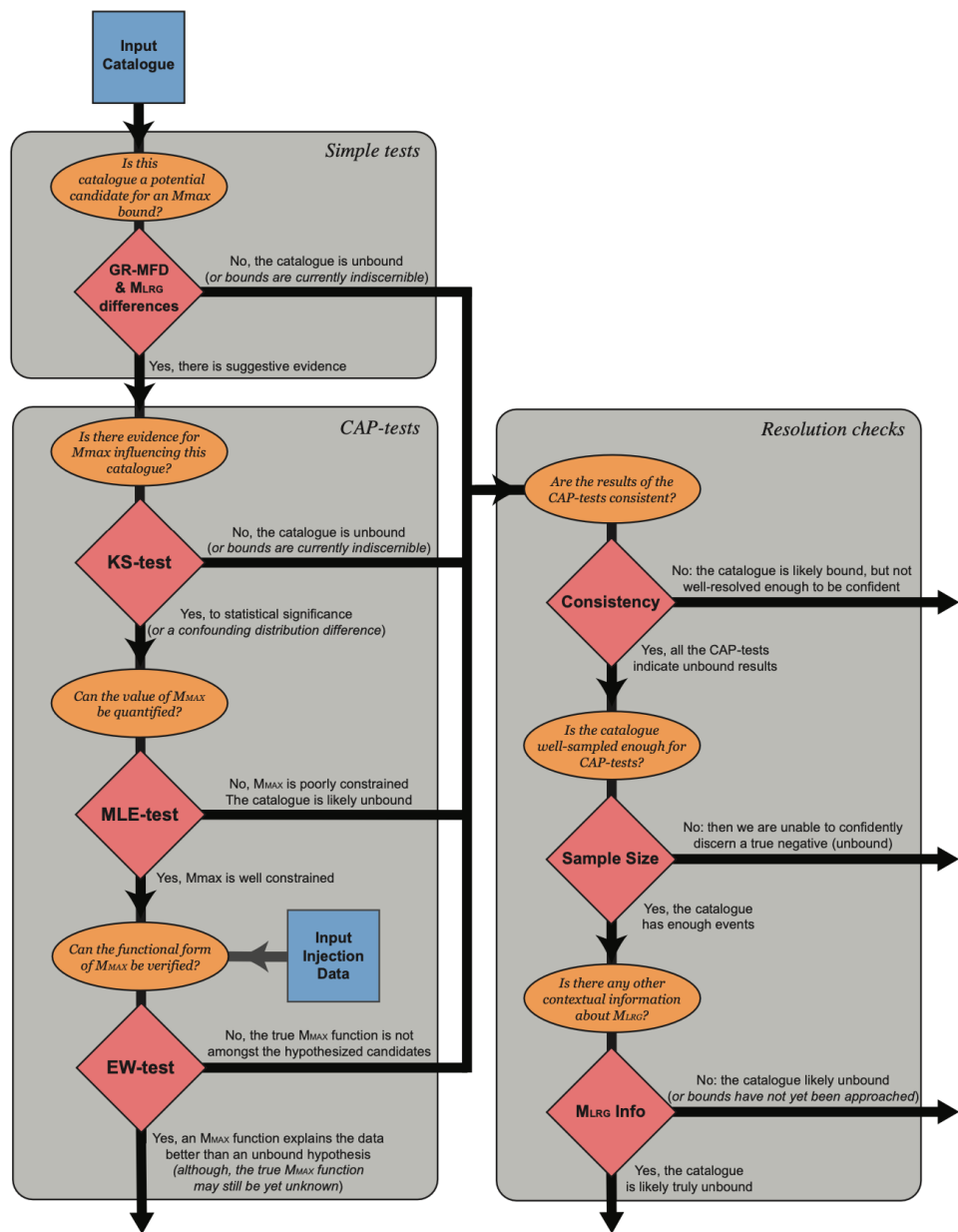


2018). We perform CAP-tests on these UGL datasets and observe both bound and unbound stimulation stages. We cross-reference these observations against the wealth of geophysical observations and interpretations from prior multi-disciplinary studies. Bound cases tend to occur when stimulation is restricted to the growth of new fractures, while unbound cases tend to reactivate (relatively large) pre-existing faults/fractures. Furthermore, we empirically search for the functional form of  $M_{MAX}$  models; we delineate four categories that are predominantly consistent with theoretical expectations. Finally, we discuss how these results create a consistent picture with field-scale results.

## 2. Methods

### 2.1 Methodological Overview

The methods of this paper concern the robust inference and estimation of  $M_{MAX}$  from a catalogue of earthquakes. To do so, we have composed a suite of statistical tests. First, simple-tests can be used to pre-screen cases and provide qualitative or semi-quantitative inferences of  $M_{MAX}$  bounds. Candidate catalogues can then be examined more deeply using CAP-tests, which use a series of statistical tests to robustly discern the presence of  $M_{MAX}$  and quantify the best model hypothesis. Last, we outline criteria for assessing the absence of  $M_{MAX}$ . These tests are used to logically guide interpretations amongst the three possibilities: that  $M_{MAX}$  bounds a catalogue, that  $M_{MAX}$  is not bounding a catalogue, or that the catalogue is not well-resolved enough to make an interpretation either way. An overview of this workflow's logical sequencing has been provided (Figure 1).



134  
135 **Figure 1. Workflow to discern  $M_{\text{MAX}}$  bounds.** Simple-tests are used to pre-screen for potentially  
136 bound catalogues. Afterwards, CAP-tests can more rigorously identify bound cases.  
137

## 138 2.2 Simple-tests

139 Here, we briefly define some simple-tests to provide an initial assessment of  $M_{\text{MAX}}$ .  
140 This is accomplished through an examination of the Gutenberg-Richter magnitude frequency



distribution (GR-MFD) (Ishimoto & Iida, 1939; Gutenberg & Richter, 1944) and discrepancies between observed largest event minus the expected largest events. This sub-section constitutes the first step in our overall workflow (Figure 1).

### 2.2.1 Fitting the Gutenberg-Richter Magnitude Frequency Distribution

The GR-MFD is a relationship that describes the amount and frequency of earthquake magnitudes:  $N = 10^a 10^{-bM}$ . The  $a$ -value describes the scaling to the total amount of earthquakes  $N$ , while the  $b$ -value is the proportionality of big-to-small events. Given a catalogue of earthquake magnitudes  $M$ , this relationship can be fit through Maximum Likelihood Estimators (Marzocchi & Sandri, 2003). For real datasets, a lower bound truncation called the magnitude-of-completeness ( $M_c$ ) is introduced to account for detection incompleteness. Many methods exist to evaluate  $M_c$  robustly, to account for the incompleteness in the detection of low magnitude events, thusly to avoid biases during the GR-MFD fitting process. In this study,  $M_c$  is selected by searching for the value that maximizes the goodness-of-fit metrics like  $R^2$  (Schultz et al., 2018) or minimizes the negative log-likelihood of the GR-MFD. In cases with a goodness-of-fit plateaus/valleys, we select the value of  $M_c$  closest to plateau start. Sometimes we are conservative in our  $M_c$  choice by selecting a value slightly larger than optimal. Note that this conservatism will have a detrimental effect on finding bound cases. The  $M_c$  value selected by this process is typically near (but skewed right-ward of) the peak bin of the non-cumulative GR-MFD.

As part of the simple indicators of  $M_{MAX}$ , a visual comparison of the GR-MFD fit against the observed data is used to qualitatively examine for the presence of  $M_{MAX}$ . Catalogues that are relatively deficient in large magnitudes (compared to their fits) are possible candidates for an  $M_{MAX}$ . We note that this deficiency in large magnitude events is a key metric for identifying if/when  $M_{MAX}$  can be constrained (Holschneider et al., 2011; Schultz, 2024).

### 2.2.2 Appraising the deficiency of large events

To provide additional semi-quantitative assessments of an  $M_{MAX}$ , we examine the empirical degree-of-truncation ( $\delta M_{LRG}$ ), which is the discrepancy between the largest observed event minus the largest expected event. The expected  $M_{LRG}$  can be estimated: if a GR-MFD is assumed, then order statistics suggests a modal value of  $M_{LRG} = M_c + \log_{10}(N)/b$  (van der Elst et al., 2016). Where  $N$  is the total number of events larger than the magnitude-of-completeness  $M_c$  and  $b$  is the previously described  $b$ -value. We can use the prior GR-MFD



fits to determine the expected value of  $M_{\text{LRG}}$  and then compare that against the observed value (*i.e.*,  $\delta M_{\text{LRG}}$ ). We also use the inverted cumulative distribution function (van der Elst et al., 2016) to determine the percentile of the  $\delta M_{\text{LRG}}$  discrepancy – or the likelihood of this degree-of-truncation occurring, assuming an unbound catalogue.

As part of the simple indicators of  $M_{\text{MAX}}$ , catalogues that exhibit negative  $\delta M_{\text{LRG}}$  suggest the presence of an  $M_{\text{MAX}}$ . We note that the  $\delta M_{\text{LRG}}$  discrepancy is a proxy metric for the resolvability of CAP-tests. Usually values of  $-0.5 M$  (or less) for  $M_{\text{LRG}} - M_{\text{MAX}}$  are required to confidently assert the presence of an  $M_{\text{MAX}}$  (Schultz, 2024). Note that this  $M_{\text{LRG}} - M_{\text{MAX}}$  difference is the expected value where quantitative inferences of  $M_{\text{MAX}}$  can start being made with 95% confidence, from theoretical considerations (Equation 15; Holschneider et al., 2011).

### 2.3 CAP-tests

The CAP-tests are a suite of statistical methods aimed at discerning the influence of  $M_{\text{MAX}}$  on a catalogue; each test is rooted in fundamentally different statistical frameworks, to ensure the robust validation of results. In this sense, when all the CAP/simple-tests suggest a similar bound/unbound result, we can be (more) confident that we have reached the right interpretation – even if there might be data/method issues.

In this sub-section, we explicitly define each of the CAP-tests. We also refer readers to a past study that defines the CAP-tests in detail, provides comprehensive sensitivity tests, and highlight real-data applications (Schultz, 2024; Schultz et al., 2025). These tests build upon the simple pre-screening assessments (Section 2.2), logically answering a sequence of questions to discern the influence of  $M_{\text{MAX}}$  more rigorously (Figure 1).

#### 2.3.1 The Kolmogorov-Smirnov test (KS-test)

The first test is rooted in the statistical framework of hypothesis testing. Here, we take advantage of the fact that the distribution of magnitudes ( $M$ ) and the distribution of jumps in the sequence of large events ( $\Delta M_{\text{LRG}}$ ) is the same if unbound, but differ when there is an  $M_{\text{MAX}}$  upper bound (Schultz, 2024). This fact ideally lends itself to hypothesis testing via the KS-test (Berger & Zhou, 2014). Given a catalogue, both  $M$  and  $\Delta M_{\text{LRG}}$  can be observed. We can then compare these two observations against each other to test if they are drawn from the same distribution (or not), via the KS-test. This approach is advantageous in that it is non-parametric – *i.e.*, it is completely data-driven and imposes no assumptions about the kind of distributions  $M$  or  $\Delta M_{\text{LRG}}$  were drawn from. Because of this, we do not need to fit the data to a GR-MFD or have any knowledge/estimates of the  $b$ -value to perform our KS-test. Confidence in the KS-





208 test is reported as compliments of standard  $p$ -values, where 95% is a common threshold used  
 209 to declare statistical significance.

210 Since this test is only interested in discerning the existence of an  $M_{\text{MAX}}$ , additional  
 211 catalogue realizations can be drawn through reshuffling the order of events. In this sense,  
 212 bootstrapping can be employed to generate numerous catalogue realizations in which the KS-  
 213 test is repeated. This provides more robust  $p$ -value estimates. Testing on both synthetic and  
 214 real datasets suggests that the KS-test is significantly more sensitive to discerning  $M_{\text{MAX}}$  than  
 215 approaches that attempt to appraise GR-MFD fits (Schultz, 2024). As well, synthetic testing  
 216 on unbound cases shows that this KS-test produces false-positives at the rate expected for a  $p$ -  
 217 value distribution (Schultz, 2024). To be able to discern the influence of  $M_{\text{MAX}}$ ,  $M_{\text{LRG}}-M_{\text{MAX}}$   
 218 discrepancies of -0.5 M or better are usually required, consistent with theoretical expectation  
 219 (Holschneider et al., 2011).

220 While this formulation of the KS-test is powerful, we also provide a word of caution  
 221 towards a potential interpretation pitfall: this method is testing for differences between the  
 222 distributions  $M$  and  $\Delta M_{\text{LRG}}$ . The presence of an  $M_{\text{MAX}}$  is one possible reason for this  
 223 difference, but others may also confound a clear interpretation (*e.g.*, temporal changes in  $b$ -  
 224 value, kinked distributions, tapered distributions). Thus, the KS-test should be suitably pre-  
 225 processed or complemented with other tests to increase the certainty of an  $M_{\text{MAX}}$  interpretation.

226

227

### 228 2.3.2 The Maximum Likelihood Estimator (MLE-test)

229 The next test is rooted in the statistical framework of Maximum Likelihood Estimation.  
 230 If there is some suggestive evidence for the existence of an  $M_{\text{MAX}}$ , the next natural step is to  
 231 quantify this value. The log-likelihood function is defined as follows:

$$232 \quad \ln(\mathcal{L}(M; \theta)) = \sum_i \ln(f_M(M; b, M_C, M_{\text{MAX}})) - \sum_j \ln(f_M(\Delta M_{\text{LRG}}; b, 0, M_{\text{MAX}} - M_{\text{LRG}}))$$

233 Where the probability density function of the GR-MFD is given by  $f_M(M)$ , with a set of model  
 234 parameters  $\theta$  (Schultz, 2024). This function essentially entails two parts: the log-likelihood  
 235 for the catalogue magnitudes  $M$  (right-hand side of equation, first term) and the log-likelihood  
 236 of the jumps in largest events  $\Delta M_{\text{LRG}}$  (right-hand side of equation, second term). The optimal  
 237 set of model parameters  $\theta$  are then solved for via numerical methods to maximize the log-  
 238 likelihood, given the observed catalogue data  $M$  and  $\Delta M_{\text{LRG}}$ . We perform this optimization in  
 239 two-steps: the first using the standard log-likelihood constrain the  $b$ -value (Marzocchi &  
 240 Sandri, 2003) (with the optimal  $M_C$  estimates) and then using the composite log-likelihood to



constrain  $M_{\text{MAX}}$ . In this study, we consider the simplest  $M_{\text{MAX}}$  variant for  $f_M(M)$ , which is a truncated GR-MFD (Schultz, 2024).

If this test is only interested in discerning a stationary value of  $M_{\text{MAX}}$ , additional catalogue realizations can be drawn through reshuffling the order of events. Similar to the KS-test, bootstrapping can be employed to generate numerous catalogue realizations in which the MLE-test is repeated. This provides more robust  $M_{\text{MAX}}$  estimates. Testing on both synthetic and real datasets suggests that the MLE-test is sensitive to quantifying  $M_{\text{MAX}}$  within a hundredth of a magnitude unit when  $M_{\text{LRG}}-M_{\text{MAX}}$  discrepancies are  $-0.5$  M or better. In cases where the MLE-test is applied to unbound catalogues, bootstrapped estimates of  $M_{\text{MAX}}$  will be much larger than  $M_{\text{LRG}}$  and standard deviations can be on the order of 1 magnitude unit or greater.

### 2.3.3 The Ensemble Weighting test (EW-test)

The third and final CAP-test is rooted in the statistical framework of likelihood inference. Together, the two prior tests provide suitable evidence for the existence of  $M_{\text{MAX}}$ . However,  $M_{\text{MAX}}$  may be a function of time or injected volume, becoming some non-stationary value throughout the catalogue duration. Certainly,  $M_{\text{MAX}}$  processes relevant for induced seismicity and hydraulic fracturing have been proposed in the past (McGarr, 2014; Hallo et al., 2014; Galis et al., 2017; Elsworth, et al., 2025; Im & Avouac, 2025; Sáez et al., 2025). In this sense, having an approach that can distinguish the best proposed  $M_{\text{MAX}}$  model (given the data) would be insightful.

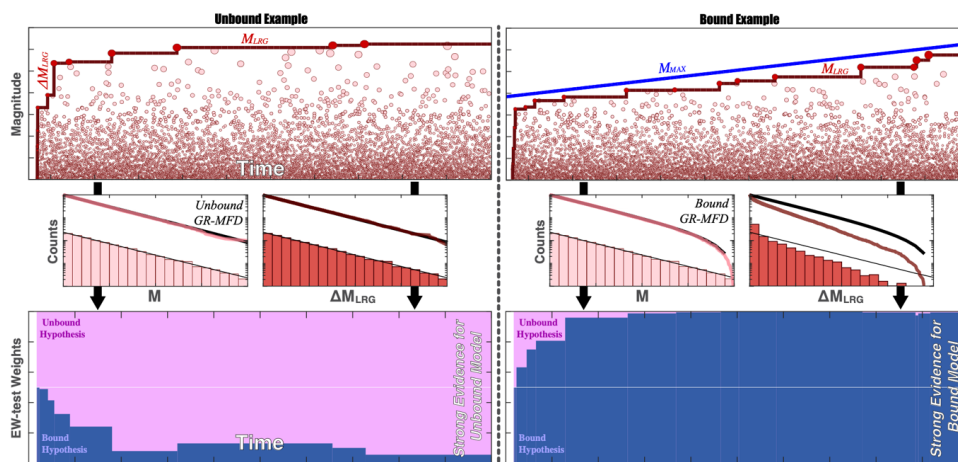
The EW-test starts by considering an ensemble of proposed  $M_{\text{MAX}}$  models to explain the catalogue data (Schultz, 2024). Using the previously defined log-likelihood function, both Akaike Information Criterion (AIC) and Bayesian Information Criterion (BIC) can be defined for each  $M_{\text{MAX}}$  model (Schwarz, 1978; Akaike, 1998); note that we have used the small sample size corrections for AIC/BIC (Sugiura, 1978; McQuarrie, 1999). Next, we compute the differences in AIC/BIC scores, by subtracting the score of the best  $M_{\text{MAX}}$  model. These score differences can be translated into relative model weights by an exponential function (Wagenmakers & Farrell, 2004). We combine AIC/BIC weights into a single weight by taking an average between the two. In this study we will consider four standard  $M_{\text{MAX}}$  models: McGarr-like (*i.e.*, log-proportional to injected volume;  $M_{\text{MAX}} \propto \log_{10}(V^1)$ ) (McGarr, 2014; Hallo et al., 2014; Elsworth, et al., 2025), Galis-like (*i.e.*,  $M_{\text{MAX}} \propto \log_{10}(V^{3/2})$ ) (Galis et al., 2017), a constant tectonic upper bound (Kanamori & Anderson, 1975), and the unbound null



274 hypothesis. The unbound null hypothesis consists of three model parameters ( $M_c$ ,  $b$ -value,  
 275 GR-MFD variance), while all bound models have one additional model parameter (*i.e.*,  $K=4$ )  
 276 to account for the slope of the volume-based relationship.

277 The interpretation of the  $M_{MAX}$  model weights is straightforward: larger model weights  
 278 indicate a better explanation of the data. The model with the largest weight is the best  
 279 explanation of the data (within the ensemble). To quantify the statistical significance of weight  
 280 differences between two models, the relative odds ratio can be computed as the ratio of the two  
 281 model weights (larger/smaller). Ratios of 1+ are insignificant, 3+ are substantial/positive, 10+  
 282 are strong, and 100+ is decisive (Kass & Raftery, 1995). We note that the best model in an  
 283 ensemble does not necessarily imply the veracity of the model; there could be another  
 284 (unknown) model that explains the data better than all of those yet considered.

285 In synthetic testing, the EW-test can accurately and confidently discern the true  $M_{MAX}$   
 286 model (Schultz, 2024). Usually, only a handful of  $\Delta M_{LRG}$  observations are required to  
 287 confidently identify the true model (*i.e.*, with odds ratios of 3-10 or better). However, like the  
 288 prior CAP-tests,  $M_{MAX}$  must be influencing the catalogue for meaningful inferences to be made.  
 289 Said another way, if the  $M_{MAX}$  is much larger than  $M_{LRG}$ , then the EW-test will not be able to  
 290 distinguish between bound/unbound hypotheses. A schematic diagram explaining the EW-test  
 291 has been provided (Figure 2).



292  
 293 **Figure 2. Schematic demonstration of the EW-test.** The upper panels show hypothetical catalogues  
 294 of earthquakes. Earthquake magnitudes ( $M$ , pink circles), the sequence of largest events ( $M_{LRG}$ , red  
 295 line), and jumps in the largest event magnitudes ( $\Delta M_{LRG}$ ) can be directly observed. Potentially, some  
 296 unobservable physical process could be bounding these catalogues ( $M_{MAX}$ , blue line). Left and right  
 297 panels detail contrasting concepts for a bound and unbound catalogue, respectively. If there is an  
 298  $M_{MAX}$ , then it can be statistically inferred from the observables. Middle panels show the differences  
 299 between distributions of  $M$  and  $M_{LRG}$ , when bounded by  $M_{MAX}$  (or not). The distribution of  $M$  follows  
 300 a GR-MFD: analytical cumulative (thick black line) and non-cumulative (thin black line) agree with



numerical cumulative (pink line) and non-cumulative (pink bars) distributions. The distribution of  $\Delta M_{\text{LRG}}$  will differ from the GR-MFD when bounded by  $M_{\text{MAX}}$ . Bottom panels show the results of EW-tests using these concepts. Weights of two hypothesized models, an unbound  $M_{\text{MAX}}$  (pink area) and a bound  $M_{\text{MAX}}$  (blue area), change as new values of  $M_{\text{LRG}}$  are observed. EW-tests can quickly infer the presence of the true  $M_{\text{MAX}}$  model, from the equivocal *a priori* assumption (white horizontal line).

## 2.4 Truly unbound or just lacking data?

In an ideal experiment, injection would continue indefinitely, providing excellent resolving power for  $M_{\text{MAX}}$  by sampling infinitely many large events near  $M_{\text{MAX}}$ . Obviously, real-data cases are sample/time-limited, however. CAP-tests have the potential to discern influence from  $M_{\text{MAX}}$  in a (sample-limited but still) well-resolved catalogue. However, an issue arises when attempting to perform these tests on poorly-resolved catalogues, since CAP-tests cannot distinguish an  $M_{\text{MAX}}$  in this case. For example, if CAP-tests fail to indicate a bound catalogue, then this could be because the catalogue is either truly unbound or simply is not well-resolved enough (*i.e.*, it has a low degree-of-truncation). Distinguishing between these two possibilities can be nebulous. We outline some guiding metrics to assist in making this assessment, which is our last workflow step in discerning the (apparent) absence of  $M_{\text{MAX}}$  more rigorously (Figure 1).

The first consideration is the consistency among simple/CAP-test results. Cases that are truly bound tend to have all tests unanimously indicate a bound process, and *vice versa*. For reference, sensitivity testing on bound real-data that was sequentially decimated indicated a loss of resolving power, consistent with the degree of decimation (Schultz et al., 2025). Specifically, the EW-test tends to lose resolving power first, followed by the KS-test, with the MLE-test generally being the most sensitive. In fact, the use of multiple sub-tests rooted in disparate statistical methods was an intentional design choice to cover strength/deficiencies of each individual approach (Schultz, 2024). Note that this consistency indicator is only relevant for semi-well-resolved cases that are truly bound; very-poorly-resolved cases would still appear as unbound.

The second metric considered is the size of the catalogue  $N$ , within 1-2 magnitude units of the current  $M_{\text{LRG}}$ . Synthetic tests indicate that catalogues between  $10^2$ - $10^3$  (above the Mc) are usually required to confidently assert  $M_{\text{MAX}}$  (Schultz, 2024). Similarly, real-data cases also noted that EW-tests can confidently assert an  $M_{\text{MAX}}$  model after observing 30-200 events – although most cases required ~50-100 events (Schultz et al., 2025). Thus, we can use catalogue size as another rough indicator for how well-resolved  $M_{\text{MAX}}$  is.



The third metric we will consider is the currently observed  $M_{LRG}$ . Specifically, we will consider  $M_{LRG}$  in a contextual comparison against relevant cases that are already known to be bound. For example, if two independent neighbouring stages (with similarly sized catalogues) give diverging bound/unbound responses, then the observed  $M_{LRG}$  can be used to make inferences. Scenarios where the unbound stage has an observed  $M_{LRG}$  greater than the bound stage is more likely to be truly unbound. On the other hand, scenarios where the unbound stage has an observed  $M_{LRG}$  significantly less than the bound stage is potentially just a poorly-resolved case.

### 3. Data, Results, & Interpretations

We apply this workflow to data collected at a few UGLs that were aimed at better understanding the hydraulic fracturing process (Figure 3). UGLs include the Äspö Hard Rock Laboratory (Äspö HRL), Sanford Underground Research Facility (SURF), and the Grimsel Test Site (GTS). Each of these UGLs had differing scopes, scales, and aims. Here, we will cover each UGL in a parallel style: we introduce each UGL, examine CAP-test results at the UGL, and then briefly interprets those results. We will start with the simpler UGLs and then transition into more complex cases, to pedagogically build upon the complexity of interpretations.

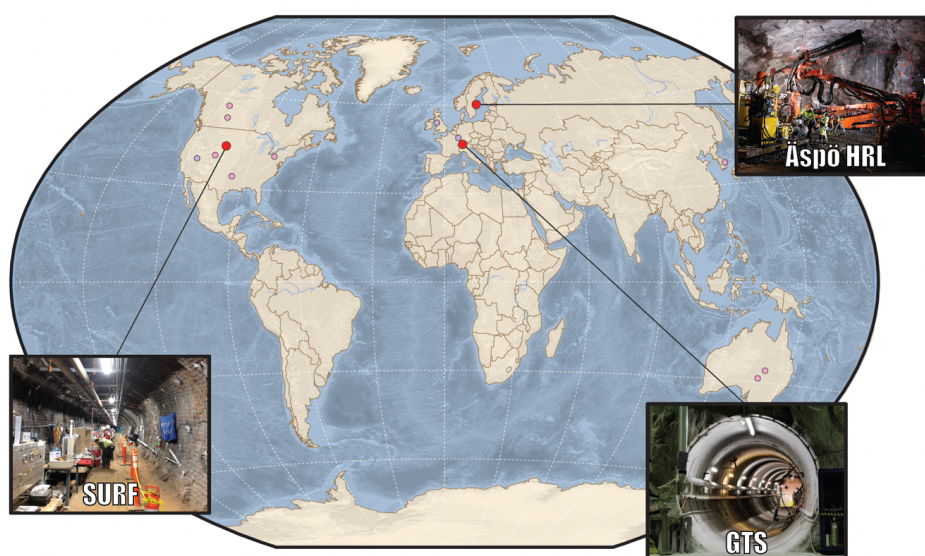


**Figure 3. Global locations of datasets.** Locations of the test sites considered: the Äspö Hard Rock Laboratory (Sweden), Sanford Underground Research Facility (South Dakota, USA), and the Grimsel



357 Test Site (Switzerland). Supporting locations from past studies (Schultz, 2024; Schultz et al., 2025),  
 358 are also shown.  
 359

### 360 **3.1 The Äspö Hard Rock Laboratory**

#### 361 3.1.1 Overview of the Äspö HRL

362 The Äspö HRL is located on the Baltic east coast of Sweden, near the Simpevarp  
 363 Peninsula (Figure 3). This UGL was constructed as a testbed to study the potential for nuclear  
 364 waste storage by the Swedish Nuclear Fuel and Waste Management Company starting in 1986.  
 365 By 1995, construction efforts reached the 450 m target depth into the granitoids of the Trans-  
 366 Scandinavian Igneous Belt (Stanfors et al., 1999).

367 The intention of recent (June 2015) injection experiments at the Äspö HRL was to test  
 368 the feasibility of cyclic stimulation as an alternative means to enhance subsurface permeability,  
 369 while also reducing the severity of induced seismicity (Zang et al., 2019; 2021). Six injection  
 370 stages (HF1-HF6) were conducted in a single borehole (28 m long at 410 m depth), with an  
 371 average stage spacing of ~3 m, and encountering either Ävrö granodiorite or fine-grained  
 372 diorite-gabbro. Stage locations were chosen to avoid natural fractures (Zimmerman et al.,  
 373 2019). Each stage used between 4.1-27.2 L of injected fluid, spread between 4-6 injection sub-  
 374 cycles (Zang et al., 2017; 2019). Some stages (HF1, HF2, HF4, & HF5) used traditional  
 375 hydraulic fracturing techniques, while other stages (HF3 & HF5) employed cyclic stimulation  
 376 (Zang et al., 2019). Resulting microseismicity was predominantly recorded in stages HF1-HF2  
 377 (López-Comino et al., 2017; Niemz et al., 2020; 2021), with events reaching up to Mw -3.5  
 378 (Kwiatek et al., 2018) and slipping with reverse or strike-slip motions (López-Comino et al.,  
 379 2021). Cyclic stimulations tended to produce less seismicity (Zang et al., 2019) and more  
 380 complex fracture networks (Stephansson et al., 2019; Zhuang et al., 2019), albeit with less  
 381 permeability enhancement (Zimmerman et al., 2019). Data for the Äspö HRL is publicly  
 382 available (Zang et al., 2024) and a spatiotemporal summary of stimulation events is plotted  
 383 (Figure 4).  
 384



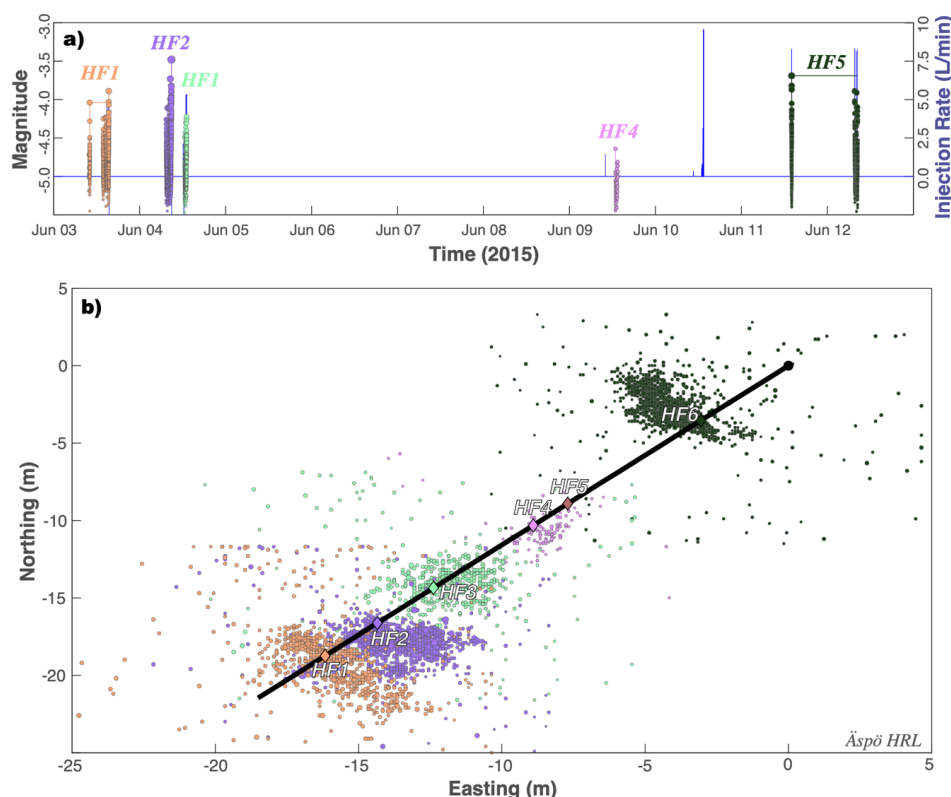


**Figure 4. Hydraulic stimulation and earthquake response at the Äspö HRL.** a) Timings and injection rates of six stages (blue line) are compared against induced earthquake magnitudes (circles). b) Locations of six stages (diamonds; HF1-HF6), along the well bore (black line), and the resultant earthquakes (circles). Injection stages and corresponding earthquakes are colour coordinated in all panels.

### 3.1.2 CAP-tests results at the Äspö HRL

To begin assessing if some process might be restricting magnitude growth at the Äspö HRL, we fit the GR-MFD to the catalogue data from each injection stage (*i.e.*, HF1-HF6). To account for magnitude errors, we employ a 50-trial bootstrap process in which the catalogue magnitudes are dithered by  $\pm 0.1$  (this includes a dithered  $M_c$ ). Only four of the stages (HF1-HF3, & HF6) have enough data to examine. Overall, the earthquakes here appear to be deficient in large-magnitude events (Figure 5). Correspondingly, the  $\delta M_{LRG}$  discrepancies range between -0.2 to -0.4 for all stages. Assuming an unbound catalogue, these degrees-of-truncation ( $\delta M_{LRG}$ ) would be  $<1^{st}$ ,  $3^{rd}$ ,  $<1^{st}$ , and  $6^{th}$  percentile events, respectively. These initial assessments are suggestive of some  $M_{MAX}$  upper bound restricting catalogue growth at the Äspö HRL.

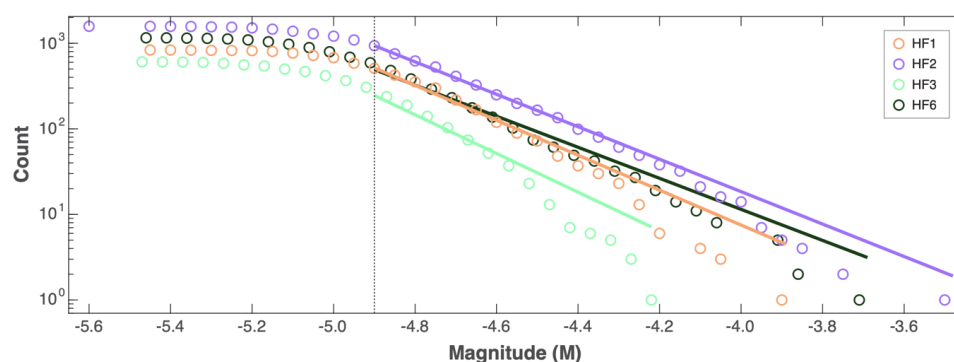


**Figure 5. Simple magnitude statistics for the Äspö HRL.** GR-MFD of cumulative events (circles), alongside best fit to the data (solid lines) and the magnitude-of-completeness (dashed line). Data is colour coordinated according to injection stages (*i.e.*, HF1-HF6).

Next, we use the CAP-tests to detect and assess the potential for  $M_{\text{MAX}}$  more rigorously. The KS-test is performed 50 times, in which the catalogue magnitudes are dithered (including a dithered truncation magnitude). The KS-test also performs 100 reshuffles within each trial. Average KS-test confidences are >99.99%, >99.99%, 99.87%, and 68.85% for stages HF1-HF3 and HF6, respectively. We perform 50 MLE-tests using dithered catalogues and 100 reshuffles within each trial. Similarly, MLE-tests suggest the standard error in fitted  $M_{\text{MAX}}$  values is 0.02, <0.01, 0.02, and 0.18 for stages HF1-HF3 and HF6, respectively. Next, we seek test hypotheses for the functional form of  $M_{\text{MAX}}$ : our EW-tests focus on McGarr-like (McGarr, 2014; Hallo et al., 2014; Elsworth, et al., 2025), the Galis-like model (Galis et al., 2017), a constant tectonic upper bound (Kanamori & Anderson, 1975), and the unbound null hypothesis. Similarly, EW-tests also show evidence for an  $M_{\text{MAX}}$  bound process, most strongly evidenced with stage HF2 (Figures 6 & S1-S3). By the end of HF2 stimulation, the Galis-like model is >100 times more likely than the unbound model (Figure 6).



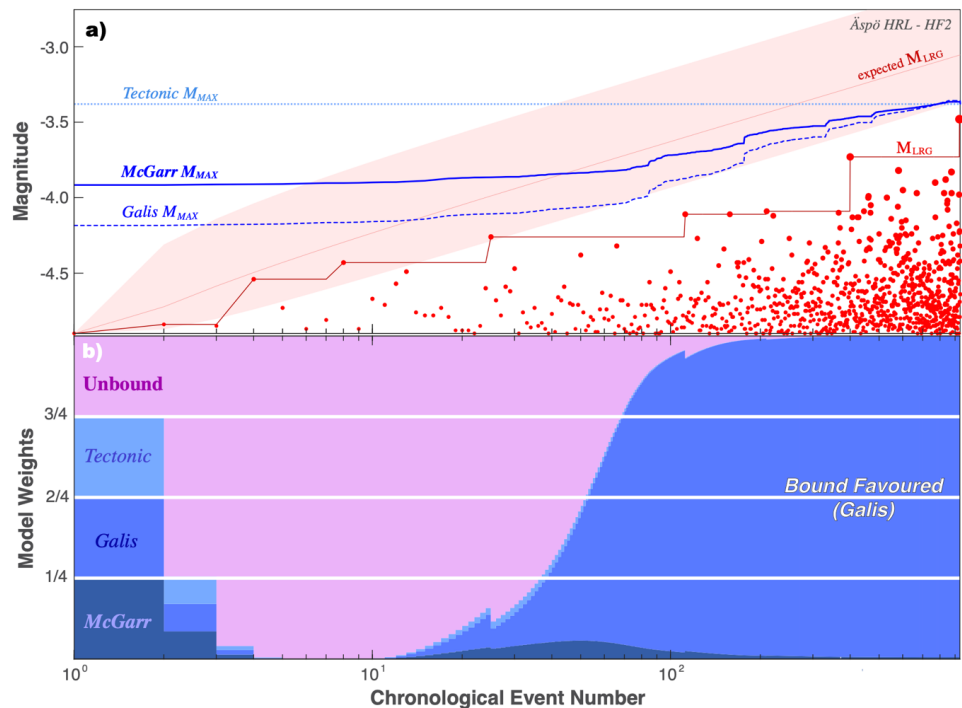


**Figure 6. Using the EW-test to discern between  $M_{MAX}$  models for HF2 at the Äspö HRL.** a) The chronological sequence of earthquake magnitudes (red circles), the observed  $M_{LRG}$  (red line), and the expected  $M_{LRG}$  at the 10/50/90 percentiles (red area) are compared against  $M_{MAX}$  hypotheses (blue lines). b) The corresponding ensemble weights update as new data is encountered.

Last, we organize our results for all injection stages at the Äspö HRL – for convenience to the reader. These results are summarized below (Table 1).

Case		Simple-tests		CAP-tests			Resolution	
UGL	Stage	$b$ -value	$\delta M_{LRG}$	KS-test	MLE-test	EW-test	$M_{MAX}$ model	$N \geq M_C$
Äspö HRL	HF2	1.71±0.08	-0.32	>99.99%	<0.01	>100	Galis	898
Äspö HRL	HF1	1.91±0.11	-0.41	>99.99%	0.02	~11	Tectonic	509
Äspö HRL	HF6	1.90±0.11	-0.24	68.85%	0.18	~0.3	Unbound	540
Äspö HRL	HF3	2.37±0.17	-0.36	99.87%	0.02	~1.3	Tectonic	265

**Table 1. Summary of results at the Äspö HRL.** All the prior results of our simple-tests and CAP-tests are compiled here for convenience. Additionally, we have coordinated individual entries according to their interpretation: blue for bound, pink for unbound, and uncoloured for indeterminate.

### 3.1.3 Interpretations for the Äspö HRL

Overall, all the stages at the Äspö HRL appear to have some evidence of a bound process restricting the growth of earthquake magnitudes. The most convincing of the cases is



also the most well-resolved one: for HF2, all the simple/CAP-tests unanimously indicate a bound process with strong statistical significance. As the cases become less well-resolved, the statistical confidence also diminishes. For example, the HF1 and HF3 stages have most CAP-tests indicating a bound process, only the EW-test of HF3 narrowly falls short of statistical significance. The HF6 stage produces the most mixed results: simple-tests, MLE-test, and EW-test are indeterminate, while the KS-test is unbound. Overall, we interpret stage HF2 as certainly being bound. Stages HF1 and HF3 as likely to be bound, but likely needing more well-resolved catalogues to better discern  $M_{MAX}$ . We hesitate to make a clear statement for HF6, which appears indeterminate due to data limitations.

The interpretation that all the Äspö HRL stages were (likely) bound corresponds with the geophysical interpretations from relevant studies. The intention of the Äspö HRL was to test various stimulation programs against the complexity/growth of hydraulic fractures (Zang et al., 2019; 2021). Stage intervals were chosen to avoid natural fractures, and impression packers noted the generation of new hydraulic fractures (Zimmerman et al., 2019). Furthermore, the progressive growth of the HF2 hydraulic fracture plane was inferred jointly from the microseismic and deformation constraints (Niemz et al., 2020; 2021). In this sense, a progressively growing fracture aligns well with the bound interpretation: the finite extent of a fracture limits  $M_{MAX}$  via geometric considerations (Kanamori & Anderson, 1975). As stimulation continues, the fracture continues to grow; thus, the value of  $M_{MAX}$  would increase alongside the injected volume. Correspondingly, each of the Äspö stages indicated bound growth (albeit with varying degrees of confidence).

These interpretations at the Äspö HRL constitute the simplest interpretation. We describe a scenario as to how hydraulic fracturing would be linked to a bound  $M_{MAX}$  interpretation. Regardless of the fracture network's complexity, the finite spatial extent of stimulated fractures ultimately restricts magnitude growth.

### 3.2 The Sanford Underground Research Facility

#### 3.2.1 Overview of the EGS Collab Experiment #1

The SURF is located near Lead, South Dakota, and has repurposed the Homestake gold mine (Figure 3). The SURF is a research facility operated by the South Dakota Science and Technology Authority to study rare-process physics (Heise, 2015). The EGS Collab takes advantage of the SURF, by using this facility to host hydraulic stimulation experiments at field-scale depths of ~1.5 km (Dobson et al., 2018; Kneafsey et al., 2018; Morris et al., 2018).



472           The EGS Collab Experiment #1 intended to connect injection and production boreholes  
473   via stimulated fractures in a controlled environment (Kneafsey et al., 2020; Morris et al., 2018).  
474   Injection and production boreholes were drilled subparallel to the estimated minimum principal  
475   stress direction (Oldenburg et al., 2017) in the phyllites of the Precambrian-aged Poorman  
476   Formation (Kneafsey et al., 2020). These metamorphic rocks are strongly foliated and highly  
477   anisotropic (Frash et al., 2019; Vigilante et al., 2017). The rock mass is generally thought to  
478   be low permeability ( $\sim 10^{-18}$  m<sup>2</sup>), with a thermally altered stress field (Singh et al., 2019). Some  
479   natural fractures were noted in borehole cores (Fu et al., 2021), with at least one noteworthy  
480   fracture that is naturally/actively flowing (Wu et al., 2021a). Starting in May 2018, stimulation  
481   stages took place at three wellbore intervals (N164, N142, N128), covering both hydraulic  
482   stimulation and hydraulic characterization programs; stimulation programs injected on the  
483   order of 10s L of water per interval (Morris et al., 2018; White et al., 2019). Resulting  
484   microseismicity was recorded for each interval, with  $\sim 2,000$  located events (Schoenball et al.,  
485   2019; 2020; Chai et al., 2020; Qin et al., 2024). Studies have covered topics including  
486   modeling heat transport (Wu et al., 2021b), strain/deformation (Guglielmi et al., 2021), and  
487   hydraulic fracture propagation (Li & Zhang, 2023). Data for the EGS Collab Experiment #1  
488   is publicly available (<https://gdr.openet.org/>) and a spatiotemporal summary of stimulation  
489   events is plotted (Figure 7).

490

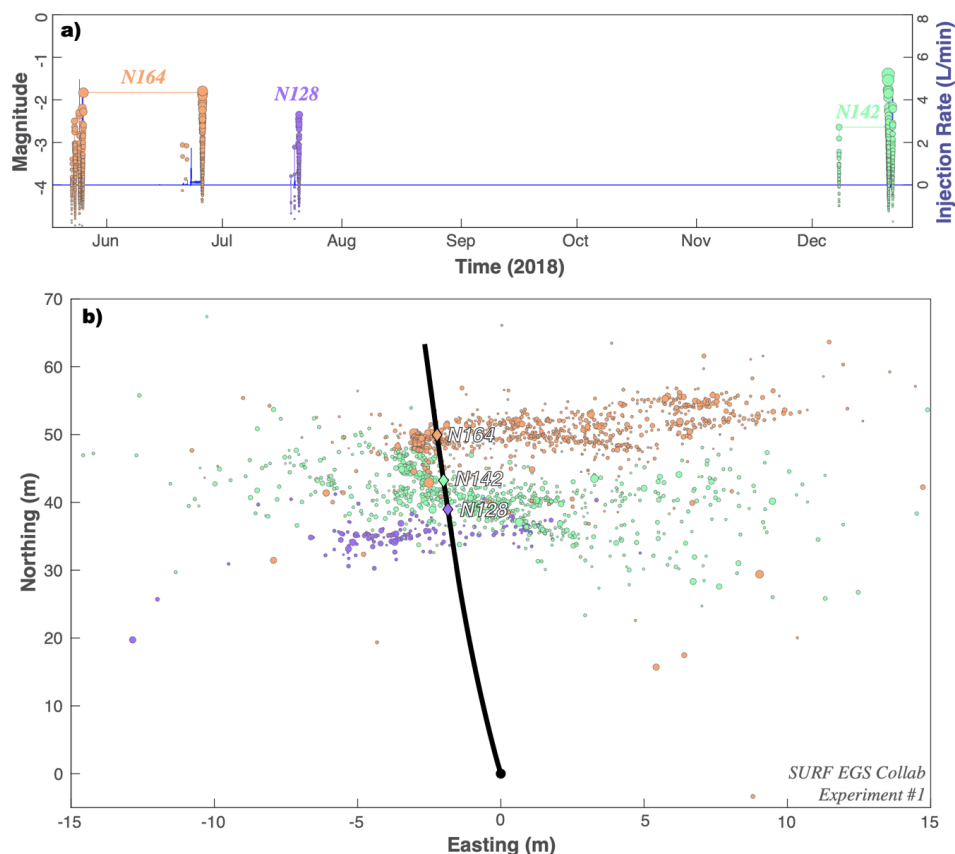


**Figure 7. Hydraulic stimulation and earthquake response for SURF Experiment #1.** a) Timings and injection rates of three stages (blue line) are compared against induced earthquake magnitudes (circles). b) Locations of three stages (diamonds; N164, N142, N128), along the well bore (black line), and the resultant earthquakes (circles). Injection stages and corresponding earthquakes are colour coordinated in all panels.

### 3.2.2 CAP-tests results from the EGS Collab Experiment #1

To begin assessing if some process might be restricting magnitude growth at SURF Experiment #1, we fit the GR-MFD to the catalogue data from each injection stage (*i.e.*, N164, N142, N128). To account for magnitude errors, we employ a 50-trial bootstrap process in which the catalogue magnitudes are dithered by  $\pm 0.1$  (this includes a dithered  $M_c$ ). Only one of the stages (N164) appear to be appreciably deficient in large magnitude events (Figure 8). Correspondingly, the  $\delta M_{LRG}$  discrepancy is significant for N164 ( $-1.15$  M), but fairly small for N142 ( $-0.05$  M) and N128 ( $-0.28$  M). Assuming an unbound catalogue, the  $\delta M_{LRG}$  discrepancy for N164 would be a  $<1^{\text{st}}$  percentile event; stages N142 ( $10^{\text{th}}$  percentile) and N128 ( $33^{\text{rd}}$  percentile).



percentile) are more commonly expected occurrences. These initial assessments are suggestive of some  $M_{MAX}$  upper bound restricting catalogue growth for one stage at SURF Experiment #1.

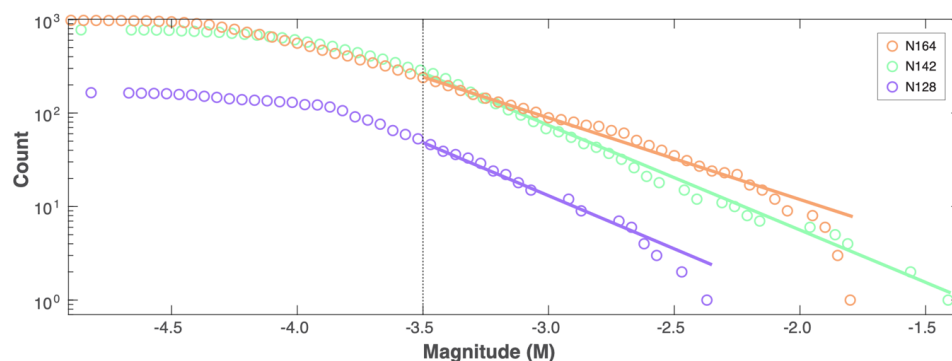


**Figure 8. Simple magnitude statistics for SURF Experiment #1.** GR-MFD of cumulative events (circles), alongside best fit to the data (solid lines) and the magnitude-of-completeness (dashed line). Data is colour coordinated according to injection stage (*i.e.*, N164, N142, N128).

Next, we use the CAP-tests to detect and assess the potential for  $M_{MAX}$  more rigorously. The KS-test is performed 50 times, in which the catalogue magnitudes are dithered (including a dithered truncation magnitude). The KS-test also performs 100 reshuffles within each trial. Again, KS-test results are split, with average confidences of 99.96% for stage N164, but 34.23% and 74.39% for stages N142 and N128, respectively. We perform 50 MLE-tests using dithered catalogues and 100 reshuffles within each trial. MLE-tests are also split: standard error in fitted  $M_{MAX}$  values are 0.10, 2.18, and 1.31 for stages N164, N142, and N128, respectively. Similarly, EW-tests also shows suggestive evidence for an  $M_{MAX}$  bound process with N164 (Figure 9), but certainly not for stages N142 and N128 (Figures S4-S5).

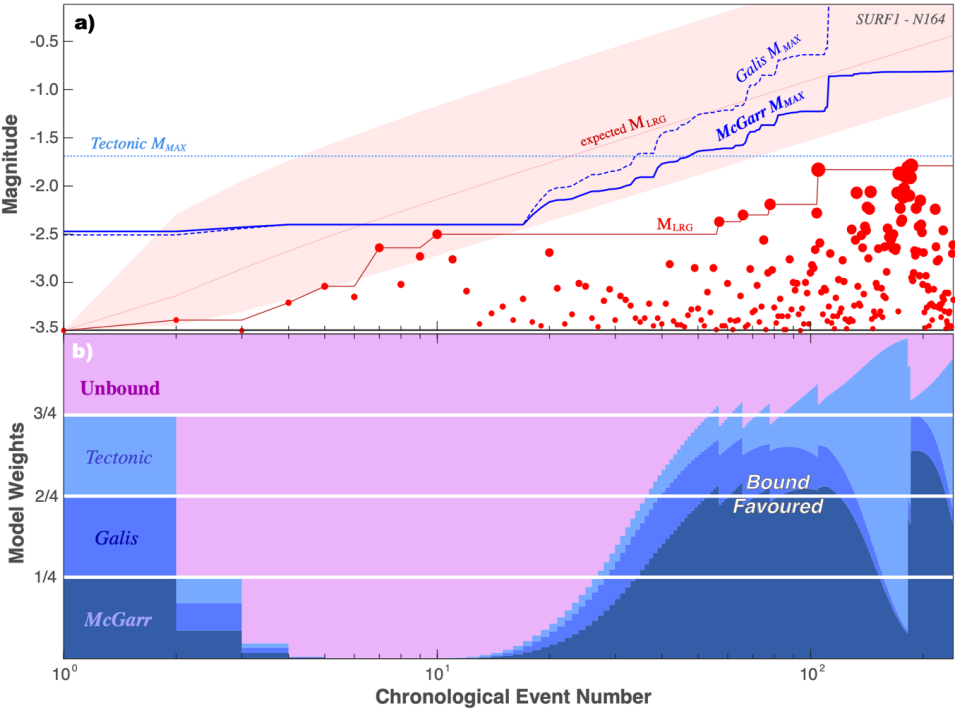


**Figure 9. Using the EW-test to discern between  $M_{MAX}$  models for N164 for SURF Experiment #1.**  
a) The chronological sequence of earthquake magnitudes (red circles), the observed  $M_{LRG}$  (red line), and the expected  $M_{LRG}$  at the 10/50/90 percentiles (red area) are compared against  $M_{MAX}$  hypotheses (blue lines). b) The corresponding ensemble weights update as new data is encountered.

Last, we organize our results for all injection stages at SURF Experiment #1 – for convenience to the reader. These results are summarized below (Table 2).

Case		Simple-tests		CAP-tests				Resolution	
UGL	Stage	$b$ -value	$\delta M_{LRG}$	KS-test	MLE-test	EW-test	$M_{MAX}$ model	$N \geq M_C$	$M_{LRG}$
SURF #1	N164	$0.83 \pm 0.02$	-1.15	99.96%	0.10	$\sim 6.0$	McGarr/Tectonic	239	-1.79
SURF #1	N142	$1.13 \pm 0.04$	-0.06	34.23%	2.18	$\sim 0.11$	Unbound	282	-1.40
SURF #1	N128	$1.18 \pm 0.05$	-0.28	74.39%	1.31	$\sim 0.04$	Unbound	50	-2.35

**Table 2. Summary of results for the SURF EGS Collab Experiment #1.** All the prior results of our simple-tests and CAP-tests are compiled here for convenience. Additionally, we have coordinated individual entries according to their interpretation: blue for bound, pink for unbound, and uncoloured for indeterminate.

### 3.2.3 Interpretations for the EGS Collab Experiment #1

CAP-test results at SURF Experiment #1 have similarities and differences from those at the Äspö HRL. For example, stage N164 is similar to the stages at the Äspö HRL: both



simple-tests and CAP-tests unanimously agree on an  $M_{MAX}$  bound – with varying degrees of confidence. On the other hand, stages N142 and N128 differ in that they produce strong and unambiguous unbound inferences. Because of this, we interpret stages N142 and N128 to be truly unbound.

The interest in considering UGL cases is the wealth of complementary geophysical information to cross-examine against the results of CAP-tests. The stimulation at stage N164 is predominantly understood to be the creation of a new fracture network. This interpretation comes from multiple lines of evidence: the orientation of microseismic fault planes with respect to the ambient stress field (Schoenball et al., 2020), deformation constraints on fracture motion (Guglielmi et al., 2021), significant recovery of injected fluid (White et al., 2019), and direct evidence of new fluid jets intersecting the producing well (Fu et al., 2021). The later N164 injections (*i.e.*, June 2018) were performed from the producing well side, into the newly created fracture network. That said, some complexity in the N164 stimulation suggested limited interaction with natural fractures, via either arrests or redirected continuation of fracture growth (Schoenball et al., 2020; Fu et al., 2021). Overall, these inferences are consistent with finite hydraulic fractures bounding the growth of earthquake magnitudes – which are the same interpretations made for the Äspö HRL.

On the other hand, stages N142 and N128 had significant interactions with natural pre-existing fractures, and likely reactivated them in shear rather than creating a new fracture network. These inferences/interpretations come from the orientation of microseismic fault planes with respect to the ambient stress field, corroboration with well image logs, and observations of shear deformation (Schoenball et al., 2020). The connection to fractures/faults allows for seemingly unbound magnitude growth, as the spatial extent of these pre-existing structures have the potential to host larger events.

These interpretations at SURF Experiment #1 constitute the next level of complexity in interpretation. We describe a scenario where hydraulic stimulation could interact with natural fractures/faults to produce an unbound process. Said another way, the interaction with natural fractures/faults (of sufficient size) can facilitate unbound magnitude growth.

### 3.3 The Grimsel Test Site

#### 3.3.1 Overview of the GTS

The GTS is located near the Grimsel pass in the central Swiss Alps (Figure 3), ~450 m below the Juchlistock in the Varsican-aged Aar Massif granites (Schneeberger et al., 2019). The GTS was established in 1984 as an underground research facility to study the safe disposal

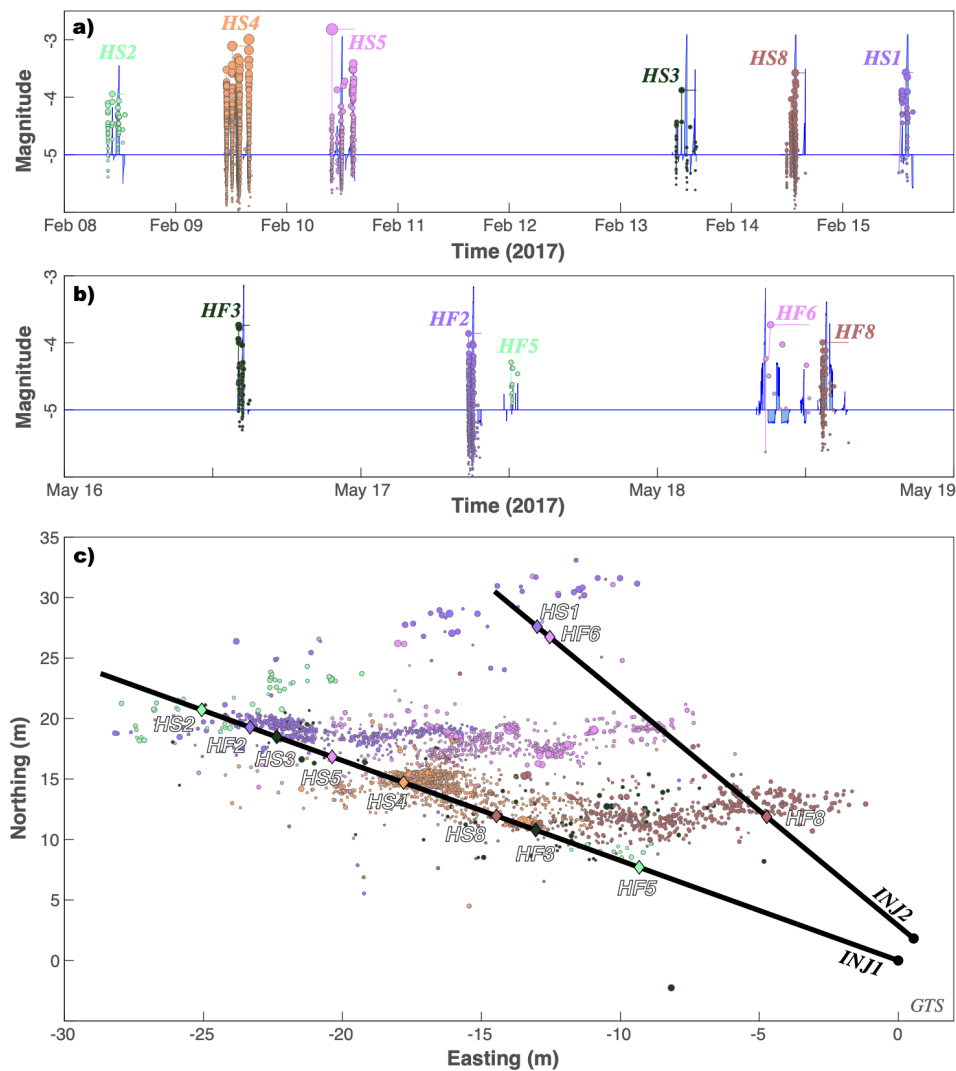


577 of nuclear waste. It is owned and operated by the National Cooperation for Radioactive Waste  
 578 Disposal (NAGRA; <https://www.grimsel.com/>).

579 The intention of recent (February-May 2017) injection experiments at the GTS was to  
 580 demonstrate the stimulation of fractures at the decameter scale and to better understand how to  
 581 manage induced seismicity (Gischig et al., 2016; Amann et al., 2018). Twelve injection stages  
 582 spanning ~1 m intervals were situated in two boreholes (~45 m long) (Gischig et al., 2020): six  
 583 related to stimulation via hydraulic fracturing (HF1-HF8) (Dutler et al., 2019) and six more via  
 584 hydroshearing (HS1-HS8) (Krietsch et al., 2020b). Each stage used (on the order of) ~1000 L  
 585 of injected fluid, spread between 4 injection sub-cycles. The role of natural faults and fractures  
 586 are a prominent focus of the GTS injection experiments, which injected into either brittle-  
 587 ductile shear zones, ductile shear zones, or intact rock (Doetsch et al., 2018a). The degree of  
 588 seismic response for individual stages was strongly heterogeneous in space, with stages HS4,  
 589 HS5, and HF2 being both the most seismically active and hosting the large events (M -3.0, M  
 590 -2.8 M, & M -3.9) (Villiger et al., 2020). Studies at the GTS were diverse, covering topics like  
 591 geological characterization (Krietsch et al., 2018a), stress inversion (Krietsch et al., 2019),  
 592 tomographic velocity changes (Doetsch et al., 2018b; Schopper et al., 2020), permeability  
 593 changes (Jalali et al., 2018; Brixel et al., 2020a; 2020b), and inferring fracture propagation  
 594 from hydromechanical response (Dutler et al., 2019; Krietsch et al., 2020a; 2020b). Data for  
 595 the GTS is publicly available (<https://doi.org/10.3929/ethz-b-000276170>) and a spatiotemporal  
 596 summary is plotted (Figure 10).

597





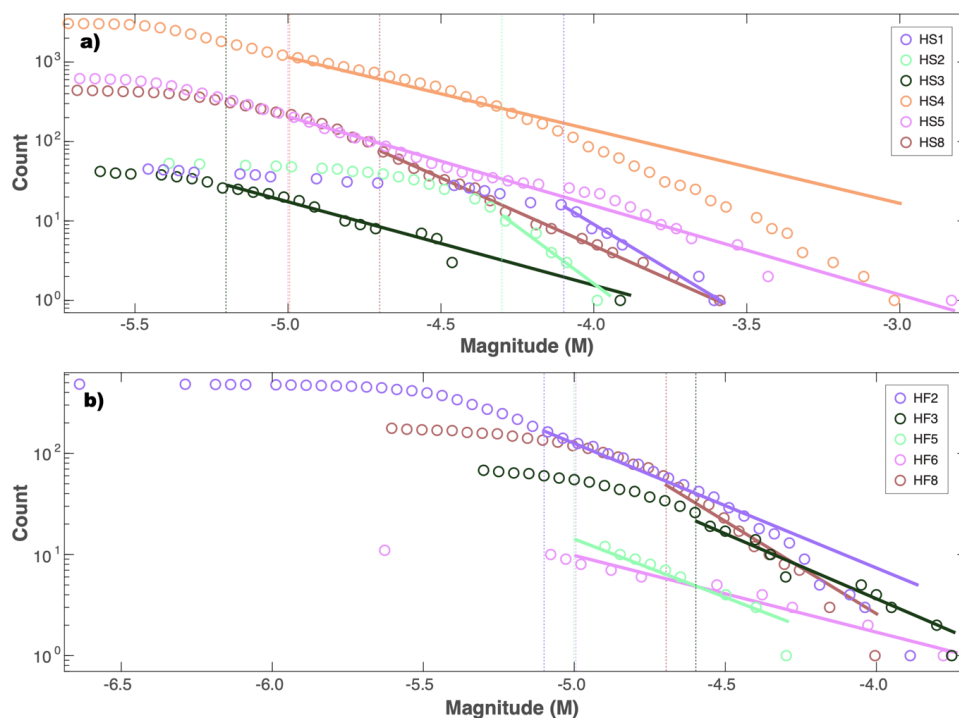
598  
599 **Figure 10. Hydraulic stimulation and earthquake response at the GTS.** a & b) Timings and  
600 injection rates of twelve stages (blue line) are compared against induced earthquake magnitudes  
601 (circles). c) Locations of twelve stages (diamonds; HFX & HSX), along the well bore (black line), and  
602 the resultant earthquakes (circles). Injection stages and corresponding earthquakes are colour  
603 coordinated in all panels.

604  
605 3.3.2 CAP-tests results at the GTS

606 To begin assessing if some process might be restricting magnitude growth at the GTS,  
607 we fit the GR-MFD to the catalogue data from each injection stage (*i.e.*, HSX & HFX). To  
608 account for magnitude errors, we employ a 50-trial bootstrap process in which the catalogue  
609 magnitudes are dithered by  $\pm 0.1$  (this includes a dithered  $M_c$ ). Note that many of the stages



610 recorded here have too few events for a meaningful analysis; thus, we predominantly focus our  
 611 discussions to a subset of stages. Only two of the stages (HS4 & HF2) appear to be appreciably  
 612 deficient in large magnitude events (Figure 11). Correspondingly, the  $\delta M_{\text{LRG}}$  discrepancy is  
 613 large for HS4 and HF2 (-1.31 M & -0.61 M), but fairly small for the other viable stages  
 614 (between -0.19 and +0.08 M). Assuming an unbound catalogue, the  $\delta M_{\text{LRG}}$  discrepancy for  
 615 HS4 and HF2 would both be  $<1^{\text{st}}$  percentile events; all other stages are commonly expected  
 616 occurrences. These initial assessments are suggestive of some  $M_{\text{MAX}}$  upper bound restricting  
 617 catalogue growth for just two stages at the GTS.  
 618

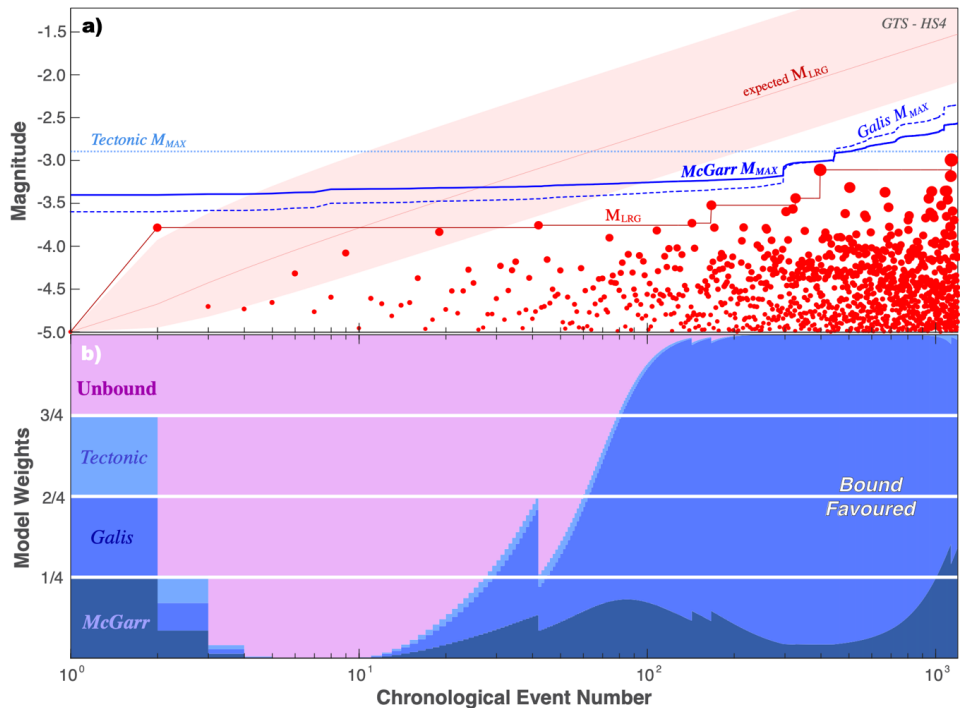


619  
 620 **Figure 11. Simple magnitude statistics at the GTS.** GR-MFD of cumulative events (circles),  
 621 alongside best fit to the data (solid lines) and the magnitude-of-completeness (dashed lines). Data is  
 622 colour coordinated according to injection stage (*i.e.*, HSX & HFX).  
 623

624 Next, we use the CAP-tests to detect and assess the potential for  $M_{\text{MAX}}$  more rigorously.  
 625 The KS-test is performed 50 times, in which the catalogue magnitudes are dithered (including  
 626 a dithered truncation magnitude). The KS-test also performs 100 reshuffles within each trial.  
 627 KS-test results are split, with strong confidences of  $>99.99\%$  for stages HS4 & HF2, but  
 628 unconvincing values for all other stages. We perform 50 MLE-tests using dithered catalogues



629 and 100 reshuffles within each trial. MLE-tests are also split: standard error in fitted  $M_{MAX}$   
630 values are  $<0.01$  and  $0.02$  for stages HS4 and HF2, but values are large ( $0.34$ - $1.92$ ) for all other  
631 stages. The EW-tests shows decisive evidence for an  $M_{MAX}$  bound process with HS4 (Figure  
632 12), and strong evidence for HF2 (Figure S6). All other stages have substantial-to-strong  
633 evidence for an unbound process via EW-tests (Figures S7-S10).  
634



635  
636 **Figure 12. Using the EW-test to discern between  $M_{MAX}$  models for HS4 at the GTS.** a) The  
637 chronological sequence of earthquake magnitudes (red circles), the observed  $M_{LRG}$  (red line), and the  
638 expected  $M_{LRG}$  at the 10/50/90 percentiles (red area) are compared against  $M_{MAX}$  hypotheses (blue  
639 lines). b) The corresponding ensemble weights update as new data is encountered.  
640

641 Last, we organize our results for all injection stages at the GTS – for convenience to  
642 the reader. These results are summarized below (Table 3).  
643

Case		Simple-tests		CAP-tests				Resolution	
UGL	Stage	$b$ -value	$\delta M_{LRG}$	KS-test	MLE-test	EW-test	$M_{MAX}$ model	$N \geq M_C$	$M_{LRG}$
GTS	HS4	$0.93 \pm 0.02$	-1.31	>99.99%	<0.01	>100	Galis	1194	-3.00
GTS	HS5	$1.11 \pm 0.05$	+0.08	32.45%	0.76	~0.07	Unbound	214	-2.82
GTS	HF2	$1.20 \pm 0.05$	-0.61	>99.99%	0.02	~60	Tectonic	170	-3.86



GTS	HS8	1.68±0.11	-0.02	71.14%	1.34	~0.15	Unbound	81	-3.58
GTS	HF8	1.97±0.14	-0.19	75.82%	0.34	~0.27	Unbound	58	-4.00
GTS	HF3	1.55±0.10	-0.06	29.02%	1.92	~0.05	Unbound	26	-3.74
GTS	HS3	1.05±0.05	-0.04	62.04%	0.98	~0.04	Unbound	26	-3.88
GTS	HS1	2.40±0.22	+0.03	46.97%	1.26	~0.01	Unbound	15	-3.57
GTS	HS2	2.76±0.38	-0.03	40.94%	0.81	~0.01	Unbound	11	-3.94
GTS	HF5	1.16±0.05	-0.22	94.34%	2.23	~0.04	Unbound	12	-4.29
GTS	HF6	0.73±0.06	-0.01	26.17%	3.61	~0.01	Unbound	9	-3.73

**Table 3. Summary of results at the GTS.** All the prior results of our simple-tests and CAP-tests are compiled here for convenience. Additionally, we have coordinated individual entries according to their interpretation: blue for bound, pink for unbound, and uncoloured for indeterminate.

### 3.3.3 Interpretations for the GTS

In summary, most of the GTS stages appear to exhibit unbound growth of earthquake magnitudes. Although, this interpretation varies in confidence, depending on the specific stage in question. The most confidently unbound case is HS5, which fails all of the simple-tests and CAP-tests. On the other hand, there are two exceptions to this general trend: HS4 shows clear and definitive evidence for a bound process, while HF2 shows strong evidence for a bound process. That said, stages with fewer than 50 events are difficult to arrive at a clear interpretation between truly unbound or simply lacking data.

The aims and scope of the GTS were to investigate the response of injection into faults/fractures at the intermediate scale (Gischig et al., 2016; Amann et al., 2018). For example, all HSX stages intentionally injected into previously known fractures of shear damage zones (Krietsch et al., 2018); thus, micro-seismically delineated fault planes were generally consistent with fracture/fault orientations (Villiger et al., 2020), near-field hydromechanical effects were consistent with pre-existing fracture dislocation (Krietsch et al., 2020b), and many stages were hydraulically connected to other boreholes via these stimulated fractures (Brixel et al., 2020b). In particular to HS5, seismicity was well fit to a single fault plane (~16 m diameter) oriented subparallel to the targeted fracture (Villiger et al., 2020), significant pressure increases (~70-75% of injection pressure) were observed in boreholes 7-8 m away (Krietsch et al., 2020a), likely due to transient permeability increases driven by fracture aperture changes (Krietsch et al., 2020b). Furthermore, the diameter of the HS5 fault plane (~16 m) is appreciably larger than the largest event diameter (~0.65 m), assuming a circular crack. HFX stages started hydraulically fracturing intact rock and subsequently propagated/stimulated new fractures (Dutler et al., 2019). However, the newly propagating fractures were inferred to have significant interactions with pre-existing fractures, which served as pressure sinks that arrested further growth (Dutler et al., 2019; Villiger et al., 2020). Note that HF6 is unique, since it



673 injected directly into a pre-existing fracture (by mistake) and thus can be considered a  
 674 hydroshearing experiment. Furthermore, the propagation of microseismic events along pipe-  
 675 like geometries was thought to be formed via the intersection with natural fractures (Dutler et  
 676 al., 2019). Given the prior interpretations of CAP-test results at SURF Experiment #1, we  
 677 would anticipate that all GTS stimulations should be unbound – because of their prominent  
 678 connection to pre-existing fractures. Bound cases would require special exceptions to this  
 679 generalization.

680 On the other hand, the HS4 stage is a clear exception to this generalization. The HS4  
 681 seismicity is not well-fit by a single plane. Instead, it is best fit by four intersecting planes (C1-  
 682 C4), where C1-C3 are oriented subparallel with pre-existing fractures and C4 is likely a new  
 683 tensile failure (Villiger et al., 2020; 2021). Clustering in focal mechanism slip style also  
 684 corresponds to spatial clusters (Villiger et al., 2021). Each cluster has seismicity spatially  
 685 restricted along discrete linear streaks (Villiger et al., 2021); these streaks grow/propagate  
 686 alongside injection, although their spatial extent (~1-2 m) is much smaller than other HSX fault  
 687 planes. In tectonic contexts, streaks are often interpreted as rheological boundaries between  
 688 seismic and creeping/locked fault segments (Rubin et al., 1999; Waldhauser et al., 2004). In  
 689 other hydraulic fracturing contexts, streaks have also been observed and analogously  
 690 interpreted (Rutledge et al., 2004; Evans et al., 2005). Thus, the streaks and clustering at HS4  
 691 has been interpreted as fractures channelizing fluid-flow towards highly seismogenic asperities  
 692 that slip perpendicular to the fluid migration direction (Villiger et al., 2021). In this sense, we  
 693 argue that HS4 seismicity is spatially bound to these asperities/streaks, giving rise to the bound  
 694 growth of magnitudes. Correspondingly, the GR-MFD for HS4 (Figure 11a) starts to roll-off  
 695 around  $M -4.3$  and  $M -3.0$  was the final  $M_{LRG}$  value; note that  $M -3.0$  roughly corresponds to a  
 696 circular crack diameter of ~0.5-1.0 m, which is comparable to the spatial extent of the streaks  
 697 (~1-2 m).

698 Similarly, HF2 is also an exception to this generalization. The HF2 seismicity was best  
 699 fit by two intersecting planes, the first which resembles a newly created hydraulic fracture and  
 700 then a deflection to a more E-W orientation (Dutler et al., 2019; Villiger et al., 2020). It has  
 701 been suggested that this stage is exceptional in that it potentially has limited interaction with  
 702 pre-existing structures, being able to propagate fracture growth before leak-off into potential  
 703 fracture connections (Dutler et al., 2019; Villiger et al., 2020). In fact, the growing hydraulic  
 704 fracture intersected monitoring boreholes, reaching further than suggested by the microseismic  
 705 events (Dutler et al., 2019). In this sense, we would argue that HF2 is most similar to the N164



stage at SURF Experiment #1. Correspondingly, both HF2 and N164 express a bound process via CAP-tests.

These interpretations at the GTS constitute the greatest level of interpretive complexity we will consider in this study. We have reiterated scenarios where hydraulic stimulation could interact with natural fractures/faults to produce an unbound process. Regardless of the stimulation program, the interaction with natural fractures/faults (of sufficient size) can facilitate unbound magnitude growth. Exceptions come in the form of hydraulic fracturing with limited interactions to natural fractures (HF2) and shear reactivation with seismicity limited to streaks/asperities (HS4).

## 4. Discussion

### 4.1 Consolidating $M_{MAX}$ interpretations

In this sub-section, we synthesize the results and interpretations of this study in comparison with relevant literature. We begin to jointly interpret the physical rationale behind bound/unbound earthquake sequences. We start by reiterating the interpretations of CAP-tests results at the UGLs and then discuss the correspondence with CAP-tests at the field-scale.

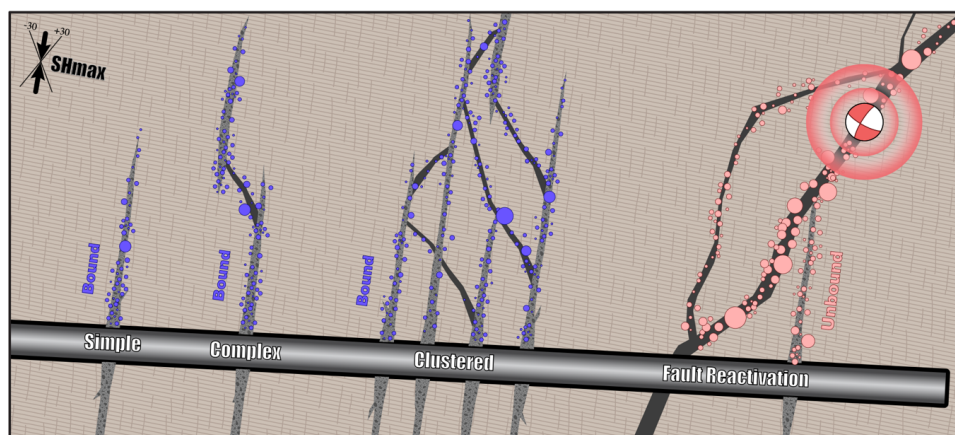
In the simplest case of the Äspö HRL (Section 3.1), stages were stimulated among intact rock, creating new hydraulic pathways via stimulated fractures. The finite geometric extent of these stimulated fractures limits the size of the largest events that can occur, at any given instant (Figure 13). Although, the spatial extent of this fracture-bound  $M_{MAX}$  will change with time/injection. Correspondingly, all Äspö HRL cases indicated a bound  $M_{MAX}$  process via CAP-tests. While newly stimulated fractures were the intention of the Äspö HRL, bound cases were also observed for analogous stages at SURF Experiment #1 (N164; Section 3.2) and the GTS (HF2; Section 3.3).

On the other hand, stages encountering more complicated interactions with pre-existing fractures/faults tended to exhibit an unbound catalogue. For example, the simplest case of fracture interaction was noted at SURF Experiment #1 (Section 3.2): the two stages (N142 & N128) that intersected a natural fracture were also unbound via CAP-tests. Furthermore, injection into faults/fractures was an aim of the GTS (Section 3.3), and these stages predominantly exhibited an unbound process. We interpret this correspondence via geometrical considerations again (Figure 13): an immediate hydraulic connection to a relatively large-scale fracture system provides an opportunity for (apparently) unrestricted magnitude growth. While we have not observed it at these three UGLs (to our knowledge), interactions with smaller-scale pre-existing fractures would be expected to produce a bound sequence.





740



741

742 **Figure 13. Interactions between stimulated fractures and reactivated faults during hydraulic**  
 743 **fracturing.** A series of stages of increasing complexity (text labels) are considered alongside a  
 744 hypothetical well (black & grey rectangle). In the simple case, the host rock is split in tension via  
 745 stimulated fractures (grey polygons). In the complex case, small pre-existing faults (black polygons)  
 746 can also be reactivated in shear slip. The clustered case hydraulically connects a series of  
 747 stages/perforations into a single fracture/fault network. In the last case, stimulated fractures intersect a  
 748 large fault system that is critically-stressed for slip. By watching the growth of earthquake magnitudes,  
 749 CAP-tests can discern between bound cases (blue circles) and unbound cases (pink circles).  
 750

751 It is worth emphasizing that stage HS4 at the GTS is exceptional (Section 3.3), in that  
 752 a bound  $M_{MAX}$  process was observed for a case with strong natural fracture interactions. Thus,  
 753 this stage is an outlier to the general interpretive theme regarding natural faults/fractures. That  
 754 said, there is also good evidence for an alternative bounding mechanism at HS4. Earthquakes  
 755 were restricted to smaller streaks along larger fault plane trends (Villiger et al., 2021); these  
 756 streaks grew in spatial extent with increased injection volume. Streaks are interpreted as fault  
 757 heterogeneity, where seismic asperities are surrounded by a broader creeping/locked fault  
 758 segment (Rubin et al., 1999; Waldhauser et al., 2004; Rutledge et al., 2004; Evans et al., 2005).  
 759 Furthermore, the spatial extent of these streaks is comparable to the fault plane area of the  
 760 largest events observed. In this sense, HS4 seismicity is likely bound to these asperities/streaks,  
 761 giving rise to the bound growth of magnitudes. Following this logic, it should be possible to  
 762 test seismic asperities for a bound  $M_{MAX}$  process (via CAP-tests) in tectonic settings too.

763 A recent study performed CAP-tests on field-scale experiments (Schultz et al., 2025),  
 764 including both shale gas hydraulic fracturing at Preston New Road in the UK (Clarke et al.,  
 765 2019; Kettlety et al., 2021) and the enhanced geothermal system at Utah FORGE (Moore et  
 766 al., 2019; Niemi et al., 2025). CAP-tests indicated that many clustered stages followed a bound



process, while the more hazardous stages were unbound. Interpretations in these field-scale cases followed a similar interpretation to UGL stages in this study (Section 4.1.1), albeit with larger uncertainties. This interpretation was partly driven by clustering sensitivity tests that showed omitting/ignoring earlier bound stages tended to diminish statistical confidence (Schultz et al., 2025) – providing an inference to the importance of accurate clustering and hydraulic connectivity for bound sequences. Certainly, natural fractures have demonstrably influenced the propagation of stimulated fractures (Jin et al., 2024). In this sense, the verification of this interpretation at UGLs provides a potential conceptual linkage to the field-scale, given their observational similarities. Prior results for bound processes are consistent with stimulating a fracture system with a restricted extent, while unbound cases likely have reactivated larger fault systems (Schultz, 2024).

#### ***4.3 Empirically constraining the functional form of $M_{MAX}$ vs $V$***

Up to this point, our study has focused on discerning between bound/unbound sequences – and establishing the importance of natural fault/fracture systems within this dichotomy. However, our discussion has neglected the underlying physical mechanisms responsible for creating this bound  $M_{MAX}$  process. Here, we further discuss the underlying physical mechanisms, for all the known bound sequences with data available (Figure 3) – both in this study and past studies (Schultz et al., 2025).

Numerous theoretical models of  $M_{MAX}$  and fracture propagation have been proposed in the literature (Eaton & Igonin, 2018). The simplest model considers a physical limitation based on the geometry of the finite fault extent (Kanamori & Anderson, 1975); For a circular fault with radius  $R$  and constant stress drop  $\Delta\sigma$ , the seismic moment release is given via the equation  $M_0 = \frac{16}{7} \Delta\sigma R^3$ . Seismic moment can then be translated into an  $M_{MAX}$  magnitude via the moment magnitude relationship (Hanks & Kanamori, 1979). Non-stationary  $M_{MAX}$  models have been proposed for induced seismicity based on the footprint of stress perturbation along a fault (Shapiro et al., 2011), the evolution of seismic moment (McGarr, 2014; Hallo et al., 2014; Elsworth et al., 2025), self-arrested rupture dynamics (Galis et al., 2017), or time-dependent pressure diffusion (Shapiro et al., 2021). Additionally, we can consider the finite extent of fracture propagation via an aseismic shear crack (Danré et al., 2024) or a tensile crack (Davis et al., 2020). These two models suggest time-varying fracture radii based on the equations  $R(t) = \sqrt{s_d V(t)}$  and  $R(t) = \sqrt[3]{k V(t)}$ , respectively.  $M_{MAX}$  models have been





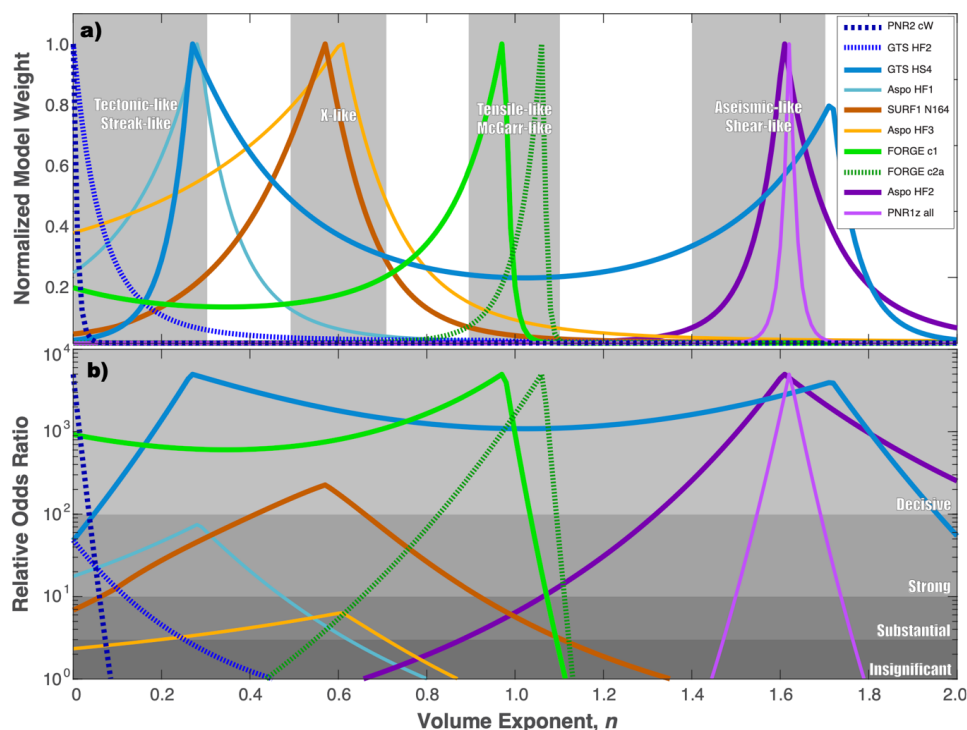
799 investigated in numerous prior studies (Kwiatek et al., 2018; Li et al., 2021; Yu et al., 2024;  
 800 Langenbruch et al., 2024; Lanza et al., 2026).

801 Examining the theoretical models illustrates a common mathematical theme: seismic  
 802 moment release ( $M_0$ ) is proportional to injected volume, raised to some exponent. For example,  
 803 the McGarr-like model considers  $M_0 \propto V^1$  (McGarr, 2014), while the Galis-like model  
 804 considers  $M_0 \propto V^{3/2}$  (Galis et al., 2017). Similarly, a growing tensile crack is equivalent to  $M_0$   
 805  $\propto V^1$  (Kanamori & Anderson, 1975; Davis et al., 2020), while a growing aseismic shear crack  
 806 is  $M_0 \propto V^{3/2}$  (Kanamori & Anderson, 1975; Danré et al., 2024; Im & Avouac, 2025; Sáez et  
 807 al., 2025). Even purely tectonic/geometric limitations can be cast into this form as  $M_0 \propto V^0$ .  
 808 Given this commonality, we consider a generic family of  $M_{\text{MAX}}$  models that have a functional  
 809 form of  $M_{\text{MAX}} \propto \log_{10}(V^n)$ . This generalization is advantageous, as the EW-test can consider  
 810 any arbitrary  $M_{\text{MAX}}$  function. Following this logic, we use these arbitrary functions within the  
 811 EW-test to find the best-fitting  $n$ -exponent for each bound case. To ensure a fair comparison,  
 812 each competing/candidate  $M_{\text{MAX}}$  model is first fit to the case data before the EW-test selects  
 813 the best model.

814 This investigation indicates that the underlying physical mechanisms are varied among  
 815 cases (Figure 14). However, the results tend to aggregate into four distinct categories:  
 816 geometric/streak-like ( $n$  0.0-0.3), X-like ( $n$  0.5-0.7), McGarr/tensile-like ( $n$  0.9-1.1), and  
 817 aseismic/shear-like ( $n$  1.4-1.7). Bounding mechanisms can be varied, even between similar  
 818 stages (*e.g.*, Äspö HRL, HF1-HF3). Higher  $n$ -exponents tend to be less confident, likely  
 819 because aseismic/shear-like exponents emulate/approach unbound-like magnitude growth (van  
 820 der Elst et al., 2016; Galis et al., 2017). Other geophysical data/studies to corroborate the  
 821 inferences of physical mechanisms are generally limited to a few cases. For example, the  
 822 propagation of microseismic events at Utah FORGE stage1-3 were best-fit by tensile-like  
 823 models (Clarkson et al., 2025; Lanza et al., 2026), which independently corresponds to our  
 824 best-fit  $n$ -exponents (0.97 & 1.06) for clusters 1 and 2 (Figure 14). Interestingly, the low  $n$ -  
 825 exponent associated with HS4 at the GTS is consistent with the observation of tectonic  
 826 streaks/asperities that exhibited limited spatial growth during injection (Villiger et al., 2021).  
 827 The X-like category is exceptional, since there is (to our knowledge) no previously suggested  
 828 model for this  $n$ -exponent. This could be potentially explained by  $M_{\text{MAX}}$  models that do not fit  
 829 the  $V^n$  generalization (Shapiro et al., 2011; 2021), an as-of-yet undiscovered  $M_{\text{MAX}}$  model, or  
 830 observational biases for encountering a relatively large pre-existing fracture network ( $V^0$ ) that  
 831 also starts growing alongside injection ( $V^1$  or  $V^{3/2}$ ). Currently, we favour the observational



832 bias interpretation for the X-like category, based on the results of drop-out tests that  
 833 demonstrate how an intermediate sized pre-existing fracture network that also grows alongside  
 834 injection can produce a mixed  $n$ -exponent with poorly-resolved data (Supplementary Section  
 835 S1 & Figure S16).



836  
 837 **Figure 14. Searching for volume-exponents.** The EW-test fit to case data (lines) for both a)  
 838 normalized model weights and b) odds ratios (relative to the unbound null hypothesis). Strength of  
 839 statistical confidence and  $n$ -exponent categories are shown with grey shaded areas (and text callouts).  
 840 Note that relative odds ratios are capped at 5000 to facilitate easier comparison via plotting.  
 841

842 Additional UGL study alongside refinements to CAP-tests (potentially also considering  
 843 other candidate  $M_{\text{MAX}}$  models) will likely shed light on the physical processes underlying  
 844 bound sequences. For example, CAP-tests could be used to systematically search for  $M_{\text{MAX}}$   
 845 models in other datasets. We note that this approach could be straightforwardly adapted to  
 846 forecast the ‘next largest event’ (Cao et al., 2020), using these weights as part of either a logic-  
 847 tree (Bommer & Verdon, 2024) or an ensemble of models (Schultz et al., 2023c).

848

#### 849 4.3 Exceptions to bound/unbound interpretations



850 Thus far, we have predominantly interpreted the difference between bound/unbound  
 851 sequences via distinctions between fracture stimulation and fault reactivation (Figure 13).  
 852 While this appears to capture the first-order effects, there likely exists subtleties that can deviate  
 853 from this conjecture.

#### 854 4.3.1 Exceptions to the bound-fracture interpretation

855 We have predominantly interpreted bound sequences arising from the finite (and  
 856 time/volume dependent) extent of a propagating fracture restricting available slip area. While  
 857 this interpretation matches both expectation and observation, we can still envision a scenario  
 858 in which a finite fracture could produce an unbound sequence. For example, in the case that  
 859 the finite extent of the fracture grows faster than the equivalent area of an unbound  $M_{LRG}$ . In  
 860 this sense, while the sequence is technically bound, it would never be empirically inferable by  
 861 magnitude information. Criteria for this condition are given below: for the  $V^n$  generalization  
 862 of  $M_{MAX}$  as well as the tensile-like and shear-like fractures. There, the expected  $M_{LRG}$   
 863 formulation is a combination of the population expectation (van der Elst et al., 2016) coupled  
 864 with a proportionality between injected volume and event counts (Shapiro et al., 2010). Note  
 865 that  $\Sigma$  is the seismogenic index, a parameter indicating a fault's potential to induce earthquakes  
 866 per unit of injected fluid volume (Shapiro et al., 2010).

$$\begin{aligned}
 868 \quad & \left(\frac{2n}{3} - \frac{1}{b}\right) \log_{10}(V(t)) + \left(\frac{2}{3}\right) \log_{10}(c) - 9.1 \gg \frac{\Sigma}{b} \\
 869 \quad & \left(1 - \frac{1}{b}\right) \log_{10}(V(t)) + \left(\frac{2}{3}\right) \log_{10}\left(\frac{16}{7} \Delta \sigma s_d^{3/2}\right) - 9.1 \gg \frac{\Sigma}{b} \\
 870 \quad & \left(\frac{2}{3} - \frac{1}{b}\right) \log_{10}(V(t)) + \left(\frac{2}{3}\right) \log_{10}\left(\frac{16}{7} \Delta \sigma k\right) - 9.1 \gg \frac{\Sigma}{b}
 \end{aligned}$$

#### 871 4.3.2 Exceptions to the unbound-fault interpretation

872 We have predominantly interpreted unbound sequences arising from fractures  
 873 interacting with relatively-large pre-existing faults. While this matches our expectation and  
 874 observations, we can still envision scenarios where pre-existing faults could produce bound  
 875 sequences. For example,  $M_{LRG}$  could be limited by the pre-existing faults being too small, the  
 876 *in situ* stress resolved on the fault (Gischig, 2015; Norbeck & Horne, 2018), time-dependence  
 877 of stress perturbations (Segall & Lu, 2015), fault geometry/complexity (Lee et al., 2024), fault  
 878 roughness (Mauer et al., 2020; Wang et al., 2024), material/stress heterogeneity (Kroll &  
 879 Cochran, 2021), rheology, or extent of asperities. In fact, HS4 at the GTS is one such  
 880 exception: where streaks outlined the rheological boundary between seismically asperities  
 881



hosted within an aseismic fault. If these factors are limiting  $M_{LRG}$ , CAP-tests should be able to discern their effects.

## 5. Conclusions

In summary, we have rigorously tested CAP-tests against data from controlled injection experiments at three underground laboratories. Bound sequences are consistent with observations of new hydraulic fracturing growth, while unbound typically reactivate larger pre-existing structures. Furthermore, the EW-test appears to be able to aggregate generalized  $M_{MAX}$  functions into categories consistent with theoretical considerations for tectonic/geometric limits, tensile/McGarr-like growth, or aseismic/shear-like growth. This process is potentially able to identify the underlying physical mechanism responsible for  $M_{MAX}$ , specific to an individual earthquake sequence. Overall, the ability to robustly identify and constrain  $M_{MAX}$  will likely be important for both induced seismicity and natural/tectonic earthquake sequences.

## Acknowledgments

We would like to thank Luigi Passarelli for insightful conversations that helped the interpretation of this study. We are grateful for the high-quality UGL studies that facilitated our CAP-test interpretations, which would have been impossible otherwise. This work is supported by the Seismogenic Fault Injection Test (SFIT), which is funded by the Swiss National Science Foundation, under project number TMPFP2\_224393. This work is also supported by the CETPartnership, which is funded by the Clean Energy Transition Partnership under the 2023 joint call for research proposals, co-funded by the European Commission (GA N°101069750) and with the funding organizations detailed on <https://cetpartnership.eu/funding-agencies-and-call-modules>.

## Data Availability

The codes (and data) used to derive our results are available online at GitHub ([LINK](#)). The catalogue and hydraulic datasets are also available online, from their source: for the Äspö HRL (Zang et al., 2024), SURF EGS Collab Experiment #1 (<https://gdr.openei.org/>), and the GTS (<https://doi.org/10.3929/ethz-b-000276170>).

## Author Contributions



915 R.S. created the CAP-tests, gathered the data, analysed the cases, and wrote the manuscript.  
916 L.V., and V.G. were involved in the curation of GTS catalogue and interpretation of the results.  
917 S.W. provided project management. All authors were involved in manuscript editing and  
918 review.

919

#### 920 **Competing Interests**

921 The authors declare no competing interests.

922

923



## References

- Akaike, H. (1998). Information theory and an extension of the maximum likelihood principle. In *Selected papers of hirotugu akaike* (pp. 199-213). New York, NY: Springer New York.
- Amann, F., Gischig, V., Evans, K., Doetsch, J., Jalali, R., Valley, B., ... & Giardini, D. (2018). The seismo-hydromechanical behavior during deep geothermal reservoir stimulations: open questions tackled in a decameter-scale in situ stimulation experiment. *Solid Earth*, 9(1), 115-137, <https://doi.org/10.5194/se-9-115-2018>.
- Atkinson, G. M., Eaton, D. W., Ghofrani, H., Walker, D., Cheadle, B., Schultz, R., ... & Kao, H. (2016). Hydraulic Fracturing and Seismicity in the Western Canada Sedimentary Basin. *Seismological Research Letters*, 87(3), 631-647, <https://doi.org/10.1785/0220150263>.
- Berger, V. W., & Zhou, Y. (2014). Kolmogorov–Smirnov test: Overview. *Wiley statsref: Statistics reference online*, <https://doi.org/10.1002/9781118445112.stat06558>.
- Bommer, J. J., Oates, S., Cepeda, J. M., Lindholm, C., Bird, J., Torres, R., ... & Rivas, J. (2006). Control of hazard due to seismicity induced by a hot fractured rock geothermal project. *Engineering Geology*, 83(4), 287-306, <https://doi.org/10.1016/j.enggeo.2005.11.002>.
- Bommer, J. J. (2022). Earthquake hazard and risk analysis for natural and induced seismicity: towards objective assessments in the face of uncertainty. *Bulletin of Earthquake Engineering*, 20(6), 2825-3069, <https://doi.org/10.1007/s10518-022-01357-4>.
- Bommer, J., & Verdon, J. P. (2024). The maximum magnitude of natural and induced earthquakes. *Geomechanics and Geophysics for Geo-Energy and Geo-Resources*, 10, 172, <https://doi.org/10.1007/s40948-024-00895-2>.
- Brixel, B., Klepikova, M., Jalali, M. R., Lei, Q., Roques, C., Kriestch, H., & Loew, S. (2020a). Tracking fluid flow in shallow crustal fault zones: 1. Insights from single-hole permeability estimates. *Journal of Geophysical Research: Solid Earth*, 125(4), e2019JB018200, <https://doi.org/10.1029/2019JB018200>.
- Brixel, B., Klepikova, M., Lei, Q., Roques, C., Jalali, M. R., Krietsch, H., & Loew, S. (2020b). Tracking fluid flow in shallow crustal fault zones: 2. Insights from cross-hole forced flow experiments in damage zones. *Journal of Geophysical Research: Solid Earth*, 125(4), e2019JB019108, <https://doi.org/10.1029/2019JB019108>.
- Cao, N. T., Eisner, L., & Jechumtálová, Z. (2020). Next record breaking magnitude for injection induced seismicity. *First Break*, 38(2), 53-57, <https://doi.org/10.3997/1365-2397.fb2020010>.
- Cao, N. T., Eisner, L., Jechumtálová, Z., Verdon, J., & Waheed, U. B. (2024). Upper limit magnitudes for induced seismicity in energy industries. *Geophysical Prospecting*, <https://doi.org/10.1111/1365-2478.13553>.
- Chai, C., Maceira, M., Santos-Villalobos, H. J., Venkatakrisnan, S. V., Schoenball, M., Zhu, W., ... & EGS Collab Team. (2020). Using a deep neural network and transfer learning to



- 973 bridge scales for seismic phase picking. *Geophysical Research Letters*, 47(16),  
 974 e2020GL088651, <https://doi.org/10.1029/2020GL088651>.  
 975
- 976 Clarke, H., Verdon, J. P., Kettlety, T., Baird, A. F., & Kendall, J. M. (2019). Real-time  
 977 imaging, forecasting, and management of human-induced seismicity at Preston New Road,  
 978 Lancashire, England. *Seismological Research Letters*, 90(5), 1902-1915,  
 979 <https://doi.org/10.1785/0220190110>.  
 980
- 981 Clarkson, C.R., Alkhayyali W., & Zeinabady, D. (2025). Characterization and modeling of  
 982 enhanced geothermal systems using methods developed for unconventional hydrocarbon  
 983 reservoirs, *SPE Annual Technical Conference and Exhibition*, SPE-228230.  
 984
- 985 Danré, P., Garagash, D., De Barros, L., Cappa, F., & Ampuero, J. P. (2024). Control of  
 986 seismicity migration in earthquake swarms by injected fluid volume and aseismic crack  
 987 propagation. *Journal of Geophysical Research: Solid Earth*, 129(1), e2023JB027276,  
 988 <https://doi.org/10.1029/2023JB027276>.  
 989
- 990 Davis, T., Rivalta, E., & Dahm, T. (2020). Critical fluid injection volumes for uncontrolled  
 991 fracture ascent. *Geophysical Research Letters*, 47(14), e2020GL087774,  
 992 <https://doi.org/10.1029/2020GL087774>.  
 993
- 994 DeDontney, N., Gans, C., Burnett, W., Burch, D., Garzon, J., Gist, G., ... & Younan, A.  
 995 (2016). Maximum magnitude of induced earthquakes in the Groningen gas field. *ExxonMobil*  
 996 *URC External Report*, [https://nam-onderzoeksrapporten.data-](https://nam-onderzoeksrapporten.data-app.nl/reports/download/groningen/en/36dea690-c7eb-4164-9d94-d9725381c426)  
 997 [app.nl/reports/download/groningen/en/36dea690-c7eb-4164-9d94-d9725381c426](https://nam-onderzoeksrapporten.data-app.nl/reports/download/groningen/en/36dea690-c7eb-4164-9d94-d9725381c426).  
 998
- 999 Dobson, P., Kneafsey, T., Morris, J., Singh, A., Zoback, M., Roggenthen, W., ... & White, M.  
 1000 (2018). The EGS Collab hydroshear experiment at the Sanford Underground Research  
 1001 Facility—Siting criteria and evaluation of candidate sites. *Geothermal Resources Council*  
 1002 *Transactions*, 42, 708-723.  
 1003
- 1004 Doetsch, J., Gischig, V., Krietsch, H., Villiger, L., Amann, F., Dutler, N., Jalali, M., Brixel,  
 1005 B., Roques, C., Giertzuch, P., Kittilä, A., and Hochreutener, R. (2018a). Grimsel ISC  
 1006 Experimental Description, *ETH Zurich Report*, <https://doi.org/10.3929/ethz-b-000310581>.  
 1007
- 1008 Doetsch, J., Gischig, V. S., Villiger, L., Krietsch, H., Nejati, M., Amann, F., ... & Giardini, D.  
 1009 (2018b). Subsurface fluid pressure and rock deformation monitoring using seismic velocity  
 1010 observations. *Geophysical Research Letters*, 45(19), 10-389,  
 1011 <https://doi.org/10.1029/2018GL079009>.  
 1012
- 1013 Dorbath, L., Cuenot, N., Genter, A., & Frogneux, M. (2009). Seismic response of the  
 1014 fractured and faulted granite of Soultz-sous-Forêts (France) to 5 km deep massive water  
 1015 injections. *Geophysical Journal International*, 177(2), 653-675,  
 1016 <https://doi.org/10.1111/j.1365-246X.2009.04030.x>.  
 1017
- 1018 Dutler, N., Valley, B., Gischig, V., Villiger, L., Krietsch, H., Doetsch, J., ... & Amann, F.  
 1019 (2019). Hydraulic fracture propagation in a heterogeneous stress field in a crystalline rock  
 1020 mass. *Solid Earth*, 10(6), 1877-1904, <https://doi.org/10.5194/se-10-1877-2019>.  
 1021





- 1022 Eaton, D. W., & Igonin, N. (2018). What controls the maximum magnitude of injection-  
1023 induced earthquakes?. *The Leading Edge*, 37(2), 135-140,  
1024 <https://doi.org/10.1190/tle37020135.1>.  
1025
- 1026 Elsworth, D., Li, Z., Yu, P., An, M., Zhang, F., Huang, R., ... & Liu, S. (2025). Constraints  
1027 on triggered seismicity and its control on permeability evolution. *Journal of Rock Mechanics*  
1028 *and Geotechnical Engineering*, 17(1), 20-30, <https://doi.org/10.1016/j.jrmge.2024.11.035>.  
1029
- 1030 Evans, K. F., Moriya, H., Niitsuma, H., Jones, R. H., Phillips, W. S., Genter, A., ... & Baria,  
1031 R. (2005). Microseismicity and permeability enhancement of hydrogeologic structures during  
1032 massive fluid injections into granite at 3 km depth at the Soultz HDR site. *Geophysical*  
1033 *Journal International*, 160(1), 388-412, <https://doi.org/10.1111/j.1365-246X.2004.02474.x>.  
1034
- 1035 Foulger, G. R., Wilson, M. P., Gluyas, J. G., Julian, B. R., & Davies, R. J. (2018). Global  
1036 review of human-induced earthquakes. *Earth-Science Reviews*, 178, 438-514,  
1037 <https://doi.org/10.1016/j.earscirev.2017.07.008>.  
1038
- 1039 Frash, L. P., Carey, J. W., & Welch, N. J. (2019, February). EGS collab experiment 1  
1040 geomechanical and hydrological properties by triaxial direct shear. In *44th workshop on*  
1041 *geothermal reservoir engineering*.  
1042
- 1043 Fu, P., Schoenball, M., Ajo-Franklin, J. B., Chai, C., Maceira, M., Morris, J. P., ... & EGS  
1044 Collab Team. (2021). Close observation of hydraulic fracturing at EGS Collab Experiment 1:  
1045 Fracture trajectory, microseismic interpretations, and the role of natural fractures. *Journal of*  
1046 *Geophysical Research: Solid Earth*, 126(7), e2020JB020840,  
1047 <https://doi.org/10.1029/2020JB020840>.  
1048
- 1049 Galis, M., Ampuero, J. P., Mai, P. M., & Cappa, F. (2017). Induced seismicity provides  
1050 insight into why earthquake ruptures stop. *Science Advances*, 3(12), eaap7528,  
1051 <https://doi.org/10.1126/sciadv.aap7528>.  
1052
- 1053 Grigoli, F., Cesca, S., Rinaldi, A. P., Manconi, A., Lopez-Comino, J. A., Clinton, J. F., ... &  
1054 Wiemer, S. (2018). The November 2017 Mw 5.5 Pohang earthquake: A possible case of  
1055 induced seismicity in South Korea. *Science*, 360(6392), 1003-1006,  
1056 <https://doi.org/10.1126/science.aat2010>.  
1057
- 1058 Gischig, V. S. (2015). Rupture propagation behavior and the largest possible earthquake  
1059 induced by fluid injection into deep reservoirs. *Geophysical Research Letters*, 42(18), 7420-  
1060 7428, <https://doi.org/10.1002/2015GL065072>.  
1061
- 1062 Gischig, V., Jalali, R., Amann, F., Krietsch, H., Klepikova, M., Esposito, S., ... & Madonna,  
1063 C. (2016). Impact of the ISC Experiment at the Grimsel Test Site-Assessment of Potential  
1064 Seismic Hazard and Disturbances to Nearby Experiments and KWO Infrastructure. *ETH*  
1065 *Zurich Report*, <https://doi.org/10.3929/ethz-b-000189973>.  
1066
- 1067 Gischig, V. S., Giardini, D., Amann, F., Hertrich, M., Krietsch, H., Loew, S., ... & Valley, B.  
1068 (2020). Hydraulic stimulation and fluid circulation experiments in underground laboratories:  
1069 Stepping up the scale towards engineered geothermal systems. *Geomechanics for Energy and*  
1070 *the Environment*, 24, 100175, <https://doi.org/10.1016/j.gete.2019.100175>.  
1071





- 1072 Guglielmi, Y., Cook, P., Soom, F., Schoenball, M., Dobson, P., & Kneafsey, T. (2021). In  
 1073 situ continuous monitoring of borehole displacements induced by stimulated hydrofracture  
 1074 growth. *Geophysical Research Letters*, 48(4), e2020GL090782,  
 1075 <https://doi.org/10.1029/2020GL090782>.  
 1076
- 1077 Gutenberg, B., & Richter, C. F. (1944). Frequency of earthquakes in California. *Bulletin of*  
 1078 *the Seismological Society of America*, 34(4), 185-188,  
 1079 <https://doi.org/10.1785/BSSA0340040185>.  
 1080
- 1081 Hanks, T. C., & Kanamori, H. (1979). A moment magnitude scale. *Journal of Geophysical*  
 1082 *Research: Solid Earth*, 84(B5), 2348-2350, <https://doi.org/10.1029/JB084iB05p02348>.  
 1083
- 1084 Hallo, M., Oprsal, I., Eisner, L., & Ali, M. Y. (2014). Prediction of magnitude of the largest  
 1085 potentially induced seismic event. *Journal of Seismology*, 18, 421-431,  
 1086 <https://doi.org/10.1007/s10950-014-9417-4>.  
 1087
- 1088 Heise, J. (2015). The Sanford underground research facility at Homestake. In *Journal of*  
 1089 *Physics: Conference Series* (Vol. 606, No. 1, p. 012015). IOP Publishing,  
 1090 <https://doi.org/10.1088/1742-6596/606/1/012015>.  
 1091
- 1092 Holschneider, M., Zöller, G., & Hainzl, S. (2011). Estimation of the maximum possible  
 1093 magnitude in the framework of a doubly truncated Gutenberg–Richter model. *Bulletin of the*  
 1094 *Seismological Society of America*, 101(4), 1649-1659, <https://doi.org/10.1785/0120100289>.  
 1095
- 1096 Holschneider, M., Zöller, G., Clements, R., & Schorlemmer, D. (2014). Can we test for the  
 1097 maximum possible earthquake magnitude?. *Journal of Geophysical Research: Solid Earth*,  
 1098 119(3), 2019-2028, <https://doi.org/10.1002/2013JB010319>.  
 1099
- 1100 Im, K., & Avouac, J. P. (2025). Maximum Magnitude of Induced Earthquakes in Rate and  
 1101 State Friction Framework. *Seismological Research Letters*, 96(3), 1654-1664,  
 1102 <https://doi.org/10.1785/0220240382>.  
 1103
- 1104 Ishimoto, M., & Iida, K. (1939). Observations of earthquakes registered with the  
 1105 microseismograph constructed recently. *Bull. Earthq. Res. Inst. Univ. Tokyo*, 17, 443-478.  
 1106
- 1107 Jalali, M., Gischig, V., Doetsch, J., Näf, R., Krietsch, H., Klepikova, M., ... & Giardini, D.  
 1108 (2018). Transmissivity changes and microseismicity induced by small-scale hydraulic  
 1109 fracturing tests in crystalline rock. *Geophysical Research Letters*, 45(5), 2265-2273,  
 1110 <https://doi.org/10.1002/2017GL076781>.  
 1111
- 1112 Jin, G., Ning, Y., Gale, M., Simmons, J., & Tura, A. (2024). Impact of natural fractures on  
 1113 hydraulic fracture propagation in Denver-Julesburg Basin: Insights from a decade of research.  
 1114 *The Leading Edge*, 43(12), 806-814, <https://doi.org/10.1190/tle43120806.1>.  
 1115
- 1116 Kanamori, H., & Anderson, D. L. (1975). Theoretical basis of some empirical relations in  
 1117 seismology. *Bulletin of the Seismological Society of America*, 65(5), 1073-1095,  
 1118 <https://doi.org/10.1785/BSSA0650051073>.  
 1119
- 1120 Kass, R. E., & Raftery, A. E. (1995). Bayes factors. *Journal of the American Statistical*  
 1121 *Association*, 90(430), 773-795, <https://doi.org/10.1080/01621459.1995.10476572>.



- 1122  
 1123 Kettlety, T., Verdon, J. P., Butcher, A., Hampson, M., & Craddock, L. (2021). High-  
 1124 resolution imaging of the ML 2.9 August 2019 earthquake in Lancashire, United Kingdom,  
 1125 induced by hydraulic fracturing during Preston New Road PNR-2 operations. *Seismological*  
 1126 *Research Letters*, 92(1), 151-169, <https://doi.org/10.1785/0220200187>.  
 1127  
 1128 Krietsch, H., Doetsch, J., Dutler, N., Jalali, M., Gischig, V., Loew, S., & Amann, F. (2018).  
 1129 Comprehensive geological dataset describing a crystalline rock mass for hydraulic  
 1130 stimulation experiments. *Scientific data*, 5(1), 1-12, <https://doi.org/10.1038/sdata.2018.269>.  
 1131  
 1132 Krietsch, H., Gischig, V., Evans, K., Doetsch, J., Dutler, N. O., Valley, B., & Amann, F.  
 1133 (2019). Stress measurements for an in situ stimulation experiment in crystalline rock:  
 1134 integration of induced seismicity, stress relief and hydraulic methods. *Rock Mechanics and*  
 1135 *Rock Engineering*, 52, 517-542, <https://doi.org/10.1007/s00603-018-1597-8>.  
 1136  
 1137 Krietsch, H., Villiger, L., Doetsch, J., Gischig, V., Evans, K. F., Brixel, B., ... & Amann, F.  
 1138 (2020a). Changing flow paths caused by simultaneous shearing and fracturing observed  
 1139 during hydraulic stimulation. *Geophysical Research Letters*, 47(3), e2019GL086135,  
 1140 <https://doi.org/10.1029/2019GL086135>.  
 1141  
 1142 Krietsch, H., Gischig, V. S., Doetsch, J., Evans, K. F., Villiger, L., Jalali, M., ... & Amann, F.  
 1143 (2020b). Hydromechanical processes and their influence on the stimulation effected volume:  
 1144 observations from a decameter-scale hydraulic stimulation project. *Solid Earth*, 11(5), 1699-  
 1145 1729, <https://doi.org/10.5194/se-11-1699-2020>.  
 1146  
 1147 Kroll, K. A., & Cochran, E. S. (2021). Stress controls rupture extent and maximum  
 1148 magnitude of induced earthquakes. *Geophysical Research Letters*, 48(11), e2020GL092148,  
 1149 <https://doi.org/10.1029/2020GL092148>.  
 1150  
 1151 Kneafsey, T. J., Dobson, P., Blankenship, D., Morris, J., Knox, H., Schwering, P., ... &  
 1152 Valladao, C. (2018). An overview of the EGS Collab project: field validation of coupled  
 1153 process modeling of fracturing and fluid flow at the Sanford Underground Research Facility,  
 1154 Lead, SD. In *43rd Workshop on Geothermal Reservoir Engineering* (Vol. 2018).  
 1155  
 1156 Kneafsey, T. J., Blankenship, D., Dobson, P. F., Morris, J. P., White, M. D., Fu, P., ... &  
 1157 Valladao, C. (2020). The EGS collab project: Learnings from Experiment 1. In *Proceedings*  
 1158 *of the 45th Workshop on Geothermal Reservoir Engineering* (pp. 10-12). Stanford, CA:  
 1159 Stanford University.  
 1160  
 1161 Kwiątek, G., Martínez-Garzón, P., Plenkers, K., Leonhardt, M., Zang, A., von Specht, S., ...  
 1162 & Bohnhoff, M. (2018). Insights into complex subdecimeter fracturing processes occurring  
 1163 during a water injection experiment at depth in Äspö Hard Rock Laboratory, Sweden.  
 1164 *Journal of Geophysical Research: Solid Earth*, 123(8), 6616-6635,  
 1165 <https://doi.org/10.1029/2017JB014715>.  
 1166  
 1167 Langenbruch, C., Moein, M. J., & Shapiro, S. A. (2024). Are maximum magnitudes of  
 1168 induced earthquakes controlled by pressure diffusion?. *Philosophical Transactions A*,  
 1169 382(2276), 20230184, <https://doi.org/10.1098/rsta.2023.0184>.  
 1170



- 1171 Lanza, F., Rinaldi, A.P., Passarelli, L., Ritz, V.A., Repollés, V.C., Schultz, R., Ciardo, F.,  
 1172 Dyer, B., Ermert, L., Grigoratos, I., Karvounis, D., Meier, P., Mignan, A., Moore, J. Pankow,  
 1173 K., Scarabello, L., Schmid, N., Shi, P., Tuinstra, K., & Wiemer, S. (2026). The 2022  
 1174 hydraulic stimulation at Utah FORGE: investigating fracturing mechanisms and testing  
 1175 forecasting approaches. Submitted to *Seismica*.  
 1176  
 1177 Lee, J., Tsai, V. C., Hirth, G., Chatterjee, A., & Trugman, D. T. (2024). Fault-network  
 1178 geometry influences earthquake frictional behaviour. *Nature*, 1-5,  
 1179 <https://doi.org/10.1038/s41586-024-07518-6>.  
 1180  
 1181 Li, Z., Elsworth, D., & Wang, C. (2021). Constraining maximum event magnitude during  
 1182 injection-triggered seismicity. *Nature Communications*, 12(1), 1528,  
 1183 <https://doi.org/10.1038/s41467-020-20700-4>.  
 1184  
 1185 Li, S., & Zhang, D. (2023). Three-dimensional thermoporoelastic modeling of  
 1186 hydrofracturing and fluid circulation in hot dry rock. *Journal of Geophysical Research: Solid*  
 1187 *Earth*, 128(2), e2022JB025673, <https://doi.org/10.1029/2022JB025673>.  
 1188  
 1189 López-Comino, J. Á., Cesca, S., Heimann, S., Grigoli, F., Milkereit, C., Dahm, T., & Zang,  
 1190 A. (2017). Characterization of hydraulic fractures growth during the Äspö Hard Rock  
 1191 Laboratory experiment (Sweden). *Rock Mechanics and Rock Engineering*, 50, 2985-3001,  
 1192 <https://doi.org/10.1007/s00603-017-1285-0>.  
 1193  
 1194 López-Comino, J. Á., Cesca, S., Niemz, P., Dahm, T., & Zang, A. (2021). Rupture directivity  
 1195 in 3D inferred from acoustic emissions events in a mine-scale hydraulic fracturing  
 1196 experiment. *Frontiers in Earth Science*, 9, 670757,  
 1197 <https://doi.org/10.3389/feart.2021.670757>.  
 1198  
 1199 Majer, E. L., Baria, R., Stark, M., Oates, S., Bommer, J., Smith, B., & Asanuma, H. (2007).  
 1200 Induced seismicity associated with enhanced geothermal systems. *Geothermics*, 36(3), 185-  
 1201 222, <https://doi.org/10.1016/j.geothermics.2007.03.003>.  
 1202  
 1203 Marzocchi, W., & Sandri, L. (2003). A review and new insights on the estimation of the b-  
 1204 value and its uncertainty. *Annals of Geophysics*, 46(6), 1271-1282.  
 1205  
 1206 Maurer, J., Dunham, E. M., & Segall, P. (2020). Role of fluid injection on earthquake size in  
 1207 dynamic rupture simulations on rough faults. *Geophysical Research Letters*, 47(13),  
 1208 e2020GL088377, <https://doi.org/10.1029/2020GL088377>.  
 1209  
 1210 McGarr, A. (2014). Maximum magnitude earthquakes induced by fluid injection. *Journal of*  
 1211 *Geophysical Research: solid earth*, 119(2), 1008-1019,  
 1212 <https://doi.org/10.1002/2013JB010597>.  
 1213  
 1214 McQuarrie, A. D. (1999). A small-sample correction for the Schwarz SIC model selection  
 1215 criterion. *Statistics & Probability Letters*, 44(1), 79-86, [https://doi.org/10.1016/S0167-](https://doi.org/10.1016/S0167-7152(98)00294-6)  
 1216 [7152\(98\)00294-6](https://doi.org/10.1016/S0167-7152(98)00294-6).  
 1217  
 1218 Mendecki, A.J., 2016. Mine Seismology Reference Book: Seismic Hazard: Institute of Mine  
 1219 Seismology, Tasmania, Australia. p 88. ISBN 978-0-9942943-0-2.  
 1220



- 1221 Moein, M. J., Langenbruch, C., Schultz, R., Grigoli, F., Ellsworth, W. L., Wang, R., ... &  
 1222 Shapiro, S. (2023). The physical mechanisms of induced earthquakes. *Nature Reviews Earth*  
 1223 *& Environment*, 4(12), 847-863, <https://doi.org/10.1038/s43017-023-00497-8>.  
 1224
- 1225 Moore, J., McLennan, J., Allis, R., Pankow, K., Simmons, S., Podgorney, R., ... & Rickard,  
 1226 W. (2019). The Utah Frontier Observatory for Research in Geothermal Energy (FORGE): an  
 1227 international laboratory for enhanced geothermal system technology development. In *44th*  
 1228 *Workshop on Geothermal Reservoir Engineering* (pp. 11-13). Stanford University.  
 1229
- 1230 Morris, J. P., Fu, P., Dobson, P., Ajo-Franklin, J., Kneafsey, T. J., Knox, H., ... & EGS  
 1231 Collab Team, \_ . (2018). Experimental design for hydrofracturing and fluid flow at the DOE  
 1232 EGS collab testbed. In *ARMA US Rock Mechanics/Geomechanics Symposium* (pp. ARMA-  
 1233 2018). ARMA.  
 1234
- 1235 Muntendam-Bos, A. G., Hoedeman, G., Polychronopoulou, K., Draganov, D., Weemstra, C.,  
 1236 van der Zee, W., ... & Roest, H. (2022). An overview of induced seismicity in the  
 1237 Netherlands. *Netherlands Journal of Geosciences*, 101, e1,  
 1238 <https://doi.org/10.1017/njg.2021.14>.  
 1239
- 1240 Niemz, P., Cesca, S., Heimann, S., Grigoli, F., von Specht, S., Hammer, C., ... & Dahm, T.  
 1241 (2020). Full-waveform-based characterization of acoustic emission activity in a mine-scale  
 1242 experiment: a comparison of conventional and advanced hydraulic fracturing schemes.  
 1243 *Geophysical Journal International*, 222(1), 189-206, <https://doi.org/10.1093/gji/ggaa127>.  
 1244
- 1245 Niemz, P., Dahm, T., Milkereit, C., Cesca, S., Petersen, G., & Zang, A. (2021). Insights into  
 1246 hydraulic fracture growth gained from a joint analysis of seismometer-derived tilt signals and  
 1247 acoustic emissions. *Journal of Geophysical Research: Solid Earth*, 126(12), e2021JB023057,  
 1248 <https://doi.org/10.1029/2021JB023057>.  
 1249
- 1250 Niemz, P., Pankow, K., Isken, M.P., Whidden, K., McLennan, J., & Moore, J. (2025).  
 1251 Mapping fracture zones with nodal geophone patches: Insights from induced microseismicity  
 1252 during the 2024 stimulations at Utah FORGE. *Seismological Research Letters*,  
 1253 <https://doi.org/10.1785/0220240300>.  
 1254
- 1255 Norbeck, J. H., & Horne, R. N. (2018). Maximum magnitude of injection-induced  
 1256 earthquakes: A criterion to assess the influence of pressure migration along faults.  
 1257 *Tectonophysics*, 733, 108-118, <https://doi.org/10.1016/j.tecto.2018.01.028>.  
 1258
- 1259 Oldenburg, C., Dobson, P., Wu, Y., Cook, P., Kneafsey, T., Nakagawa, S., ... & Heise, J.  
 1260 (2017). Hydraulic fracturing experiments at 1500 m depth in a deep mine: Highlights from  
 1261 the kISMET project, in *42nd Workshop on Geothermal Reservoir Engineering*, p. 9, Stanford  
 1262 University.  
 1263
- 1264 Pisarenko, V. F., & Rodkin, M. V. (2022). Approaches to solving the maximum possible  
 1265 earthquake magnitude (Mmax) problem. *Surveys in Geophysics*, 1-35, doi:  
 1266 <https://doi.org/10.1007/s10712-021-09673-1>.  
 1267
- 1268 Qin, Y., Li, J., Huang, L., Schoenball, M., Ajo-Franklin, J., Blankenship, D., ... & EGS  
 1269 Collab Team. (2024). Source mechanism of kHz microseismic events recorded in multiple



- 1270 boreholes at the first EGS Collab testbed. *Geothermics*, 120, 102994,  
 1271 <https://doi.org/10.1016/j.geothermics.2024.102994>.  
 1272
- 1273 Rubin, A. M., Gillard, D., & Got, J. L. (1999). Streaks of microearthquakes along creeping  
 1274 faults. *Nature*, 400(6745), 635-641, <https://doi.org/10.1038/23196>.  
 1275
- 1276 Rutledge, J. T., Phillips, W. S., & Mayerhofer, M. J. (2004). Faulting induced by forced fluid  
 1277 injection and fluid flow forced by faulting: An interpretation of hydraulic-fracture  
 1278 microseismicity, Carthage Cotton Valley gas field, Texas. *Bulletin of the Seismological*  
 1279 *Society of America*, 94(5), 1817-1830, <https://doi.org/10.1785/012003257>.  
 1280
- 1281 Sáez, A., Passelègue, F., & Lecampion, B. (2025). Maximum size and magnitude of  
 1282 injection-induced slow slip events. *Science Advances*, 11(19), eadq0662,  
 1283 <https://doi.org/10.1126/sciadv.adq0662>.  
 1284
- 1285 Schneeberger, R., Kober, F., Spillmann, T., Blechschmidt, I., Lanyon, G. W., & Mäder, U. K.  
 1286 (2019). Grimsel Test Site: Revisiting the site-specific geoscientific knowledge. *NAGRA*  
 1287 *Technical Report 19-01*. <https://nagra.ch/en/downloads/technical-report-ntb-19-01-2/>.  
 1288
- 1289 Schoenball, M., Ajo-Franklin, J., Fu, P., & Templeton, D. (2019). *Microseismic monitoring*  
 1290 *of meso-scale stimulations for the DOE EGS Collab project at the Sanford Underground*  
 1291 *Research Facility* (No. LLNL-CONF-767025). Lawrence Livermore National Lab.(LLNL),  
 1292 Livermore, CA (United States).  
 1293
- 1294 Schoenball, M., Ajo-Franklin, J. B., Blankenship, D., Chai, C., Chakravarty, A., Dobson, P.,  
 1295 ... & EGS Collab Team. (2020). Creation of a mixed-mode fracture network at mesoscale  
 1296 through hydraulic fracturing and shear stimulation. *Journal of Geophysical Research: Solid*  
 1297 *Earth*, 125(12), e2020JB019807, <https://doi.org/10.1029/2020JB019807>.  
 1298
- 1299 Schopper, F., Doetsch, J., Villiger, L., Krietsch, H., Gischig, V. S., Jalali, M., ... & Maurer,  
 1300 H. (2020). On the variability of pressure propagation during hydraulic stimulation based on  
 1301 seismic velocity observations. *Journal of Geophysical Research: Solid Earth*, 125(2),  
 1302 e2019JB018801, <https://doi.org/10.1029/2019JB018801>.  
 1303
- 1304 Schultz, R., Atkinson, G., Eaton, D. W., Gu, Y. J., & Kao, H. (2018). Hydraulic fracturing  
 1305 volume is associated with induced earthquake productivity in the Duvernay play. *Science*,  
 1306 359(6373), 304-308, <https://doi.org/10.1126/science.aao0159>.  
 1307
- 1308 Schultz, R., Skoumal, R. J., Brudzinski, M. R., Eaton, D., Baptie, B., & Ellsworth, W. (2020).  
 1309 Hydraulic fracturing-induced seismicity. *Reviews of Geophysics*, 58(3), e2019RG000695,  
 1310 <https://doi.org/10.1029/2019RG000695>.  
 1311
- 1312 Schultz, R., Beroza, G. C., & Ellsworth, W. L. (2021a). A risk-based approach for managing  
 1313 hydraulic fracturing-induced seismicity. *Science*, 372(6541), 504-507,  
 1314 <https://doi.org/10.1126/science.abg5451>.  
 1315
- 1316 Schultz, R., Beroza, G. C., & Ellsworth, W. L. (2021b). A strategy for choosing red-light  
 1317 thresholds to manage hydraulic fracturing induced seismicity in North America. *Journal of*  
 1318 *Geophysical Research: Solid Earth*, 126(12), e2021JB022340,  
 1319 <https://doi.org/10.1029/2021JB022340>.





- 1320  
 1321 Schultz, R., Ellsworth, W. L., & Beroza, G. C. (2022). Statistical bounds on how induced  
 1322 seismicity stops. *Scientific Reports*, 12(1), 1184, [https://doi.org/10.1038/s41598-022-05216-](https://doi.org/10.1038/s41598-022-05216-9)  
 1323 [9](https://doi.org/10.1038/s41598-022-05216-9).  
 1324  
 1325 Schultz, R., Baptie, B., Edwards, B., & Wiemer, S. (2023a). Red-light thresholds for induced  
 1326 seismicity in the UK. *Seismica*, 2(2), <https://doi.org/10.26443/seismica.v2i2.1086>.  
 1327  
 1328 Schultz, R., Park, Y., Aguilar Suarez, A. L., Ellsworth, W. L., & Beroza, G. C. (2023b). En  
 1329 echelon faults reactivated by wastewater disposal near Musreau Lake, Alberta. *Geophysical*  
 1330 *Journal International*, 235(1), 417-429, <https://doi.org/10.1093/gji/ggad226>.  
 1331  
 1332 Schultz, R., Ellsworth, W. L., & Beroza, G. C. (2023c). An ensemble approach to  
 1333 characterizing trailing-induced seismicity. *Seismological Research Letters*, 94(2A), 699-707,  
 1334 <https://doi.org/10.1785/0220220352>.  
 1335  
 1336 Schultz, R. (2024). Inferring maximum magnitudes from the ordered sequence of large  
 1337 earthquakes. *Philosophical Transactions A*, 382(2276), 20230185,  
 1338 <https://doi.org/10.1098/rsta.2023.0185>.  
 1339  
 1340 Schultz, R. (2025). Reining-in the spring-slider with reinforcement learning. *Journal of*  
 1341 *Geophysical Research: Solid Earth*, 130(3), e2024JB029697,  
 1342 <https://doi.org/10.1029/2024JB029697>.  
 1343  
 1344 Schultz, R., Lanza, F., Dyer, B., Karvounis, D., Fiori, R., Shi, P., Ritz, V., Villiger, L., Meier,  
 1345 P., & Wiemer, S. (2025). The bound growth of induced earthquakes could de-risk hydraulic  
 1346 fracturing. *Communications Earth & Environment*, [https://doi.org/10.1038/s43247-025-](https://doi.org/10.1038/s43247-025-02881-2)  
 1347 [02881-2](https://doi.org/10.1038/s43247-025-02881-2).  
 1348  
 1349 Schwarz, G. (1978). Estimating the dimension of a model. *The Annals of Statistics*, 461-464.  
 1350  
 1351 Segall, P., & Lu, S. (2015). Injection-induced seismicity: Poroelastic and earthquake  
 1352 nucleation effects. *Journal of Geophysical Research: Solid Earth*, 120(7), 5082-5103,  
 1353 <https://doi.org/10.1002/2015JB012060>.  
 1354  
 1355 Shapiro, S. A., Dinske, C., Langenbruch, C., & Wenzel, F. (2010). Seismogenic index and  
 1356 magnitude probability of earthquakes induced during reservoir fluid stimulations. *The*  
 1357 *Leading Edge*, 29(3), 304-309, <https://doi.org/10.1190/1.3353727>.  
 1358  
 1359 Shapiro, S. A., Krüger, O. S., Dinske, C., & Langenbruch, C. (2011). Magnitudes of induced  
 1360 earthquakes and geometric scales of fluid-stimulated rock volumes. *Geophysics*, 76(6),  
 1361 WC55-WC63, <https://doi.org/10.1190/geo2010-0349.1>.  
 1362  
 1363 Shapiro, S. A., Kim, K. H., & Ree, J. H. (2021). Magnitude and nucleation time of the 2017  
 1364 Pohang Earthquake point to its predictable artificial triggering. *Nature Communications*,  
 1365 12(1), 6397, <https://doi.org/10.1038/s41467-021-26679-w>.  
 1366  
 1367 Singh, A., Neupane, G., Dobson, P., Zoback, M., Morris, J., Fu, P., ... & Johnston, B. (2019).  
 1368 *Slip tendency analysis of fracture networks to determine suitability of candidate testbeds for*



- 1369 *the EGS Collab hydroshear experiment* (No. INL/CON-19-53585-Rev001). Idaho National  
 1370 Laboratory, Idaho Falls, United States.  
 1371
- 1372 Stanfors, R., Rhén, I., Tullborg, E. L., & Wikberg, P. (1999). Overview of geological and  
 1373 hydrogeological conditions of the Äspö hard rock laboratory site. *Applied Geochemistry*,  
 1374 14(7), 819-834, [https://doi.org/10.1016/S0883-2927\(99\)00022-0](https://doi.org/10.1016/S0883-2927(99)00022-0).  
 1375
- 1376 Stephansson, O., Semikova, H., Zimmermann, G., & Zang, A. (2019). Laboratory pulse test  
 1377 of hydraulic fracturing on granitic sample cores from Äspö HRL, Sweden. *Rock Mechanics*  
 1378 *and Rock Engineering*, 52, 629-633, <https://doi.org/10.1007/s00603-018-1421-5>.  
 1379
- 1380 Sugiura, N. (1978). Further analysis of the data by Akaike's information criterion and the  
 1381 finite corrections. *Communications in Statistics-Theory and Methods*, 7(1), 13-26,  
 1382 <https://doi.org/10.1080/03610927808827599>.  
 1383
- 1384 van der Elst, N. J., Page, M. T., Weiser, D. A., Goebel, T. H., & Hosseini, S. M. (2016).  
 1385 Induced earthquake magnitudes are as large as (statistically) expected. *Journal of*  
 1386 *Geophysical Research: Solid Earth*, 121(6), 4575-4590,  
 1387 <https://doi.org/10.1002/2016JB012818>.  
 1388
- 1389 Verdon, J. P., & Bommer, J. J. (2021). Green, yellow, red, or out of the blue? An assessment  
 1390 of Traffic Light Schemes to mitigate the impact of hydraulic fracturing-induced seismicity.  
 1391 *Journal of Seismology*, 25, 301-326, <https://doi.org/10.1007/s10950-020-09966-9>.  
 1392
- 1393 Verdon, J.P., Pullen, B., & Rodríguez-Pradilla, G. (2023). Growth and stabilisation of  
 1394 induced seismicity rates during long-term, low pressure fluid injection. *Philosophical*  
 1395 *Transactions A*, 382(2276), 20230183, <https://doi.org/10.1098/rsta.2023.0183>.  
 1396
- 1397 Verdon, J. P., & Eisner, L. (2024). An Empirically Constrained Forecasting Strategy for  
 1398 Induced Earthquake Magnitudes Using Extreme Value Theory. *Seismological Research*  
 1399 *Letters*, <https://doi.org/10.1785/0220240061>.  
 1400
- 1401 Vigilante, P. J., Sone, H., Wang, H. F., Haimson, B., & Doe, T. W. (2017, June). Anisotropic  
 1402 strength of Poorman Formation rocks, KISMET project. In *ARMA US Rock*  
 1403 *Mechanics/Geomechanics Symposium* (pp. ARMA-2017). ARMA.  
 1404
- 1405 Villiger, L., Gischig, V. S., Doetsch, J., Krietsch, H., Dutler, N. O., Jalali, M., ... & Wiemer,  
 1406 S. (2020). Influence of reservoir geology on seismic response during decameter-scale  
 1407 hydraulic stimulations in crystalline rock. *Solid Earth*, 11(2), 627-655,  
 1408 <https://doi.org/10.5194/se-11-627-2020>.  
 1409
- 1410 Villiger, L., Gischig, V. S., Kwiatak, G., Krietsch, H., Doetsch, J., Jalali, M., ... & Wiemer, S.  
 1411 (2021). Metre-scale stress heterogeneities and stress redistribution drive complex fracture slip  
 1412 and fracture growth during a hydraulic stimulation experiment. *Geophysical Journal*  
 1413 *International*, 225(3), 1689-1703, <https://doi.org/10.1093/gji/ggab057>.  
 1414
- 1415 Wang, L., Kwiatak, G., Renard, F., Guérin-Marthe, S., Rybacki, E., Bohnhoff, M., ... &  
 1416 Dresen, G. (2024). Fault roughness controls injection-induced seismicity. *Proceedings of the*  
 1417 *National Academy of Sciences*, 121(3), e2310039121,  
 1418 <https://doi.org/10.1073/pnas.2310039121>.





- 1419  
 1420 Wagenmakers, E. J., & Farrell, S. (2004). AIC model selection using Akaike weights.  
 1421 *Psychonomic Bulletin & Review*, 11, 192-196, <https://doi.org/10.3758/BF03206482>.  
 1422  
 1423 White, M., Johnson, T., Kneafsey, T., Blankenship, D., Fu, P., Wu, H., ... & Zhang, Y. (2019,  
 1424 February). The necessity for iteration in the application of numerical simulation to EGS:  
 1425 Examples from the EGS Collab test bed 1. In *44th Workshop on Geothermal Reservoir*  
 1426 *Engineering*.  
 1427  
 1428 Waldhauser, F., Ellsworth, W. L., Schaff, D. P., & Cole, A. (2004). Streaks, multiplets, and  
 1429 holes: High-resolution spatio-temporal behavior of Parkfield seismicity. *Geophysical*  
 1430 *Research Letters*, 31(18), <https://doi.org/10.1029/2004GL020649>.  
 1431  
 1432 Wu, H., Fu, P., Morris, J. P., Mattson, E. D., Neupane, G., Smith, M. M., ... & EGS Collab  
 1433 Team. (2021a). Characterization of flow and transport in a fracture network at the EGS  
 1434 Collab field experiment through stochastic modeling of tracer recovery. *Journal of*  
 1435 *Hydrology*, 593, 125888, <https://doi.org/10.1016/j.jhydrol.2020.125888>.  
 1436  
 1437 Wu, H., Fu, P., Frone, Z., White, M. D., Ajo-Franklin, J. B., Morris, J. P., ... & EGS Collab  
 1438 Team. (2021b). Modeling heat transport processes in enhanced geothermal systems: A  
 1439 validation study from EGS Collab Experiment 1. *Geothermics*, 97, 102254,  
 1440 <https://doi.org/10.1016/j.geothermics.2021.102254>.  
 1441  
 1442 Yin, X., Jiang, C., Yin, F., Zhai, H., Zheng, Y., Wu, H., ... & Li, J. (2024). Assessment and  
 1443 optimization of maximum magnitude forecasting models for induced seismicity in enhanced  
 1444 geothermal systems: The Gonghe EGS project in Qinghai, China. *Tectonophysics*, 886,  
 1445 230438, <https://doi.org/10.1016/j.tecto.2024.230438>.  
 1446  
 1447 Yu, J., Eijssink, A., Marone, C., Rivière, J., Shokouhi, P., & Elsworth, D. (2024). Role of  
 1448 critical stress in quantifying the magnitude of fluid-injection triggered earthquakes. *Nature*  
 1449 *Communications*, 15(1), 7893, <https://doi.org/10.1038/s41467-024-52089-9>.  
 1450  
 1451 Zang, A., Zimmermann, G., Hofmann, H., Stephansson, O., Min, K. B., & Kim, K. Y.  
 1452 (2019). How to reduce fluid-injection-induced seismicity. *Rock Mechanics and Rock*  
 1453 *Engineering*, 52, 475-493, <https://doi.org/10.1007/s00603-018-1467-4>.  
 1454  
 1455 Zang, A., Zimmermann, G., Hofmann, H., Niemz, P., Kim, K. Y., Diaz, M., ... & Yoon, J. S.  
 1456 (2021). Relaxation damage control via fatigue-hydraulic fracturing in granitic rock as inferred  
 1457 from laboratory-, mine-, and field-scale experiments. *Scientific reports*, 11(1), 6780,  
 1458 <https://doi.org/10.1038/s41598-021-86094-5>.  
 1459  
 1460 Zang, A., Niemz, P., von Specht, S., Zimmermann, G., Milkereit, C., Plenkers, K., & Klee,  
 1461 G. (2024). Comprehensive data set of in situ hydraulic stimulation experiments for  
 1462 geothermal purposes at the Äspö Hard Rock Laboratory (Sweden). *Earth System Science*  
 1463 *Data*, 16(1), 295-310, <https://doi.org/10.5194/essd-16-295-2024>.  
 1464  
 1465 Zhou, W., Lanza, F., Grigoratos, I., Schultz, R., Cousse, J., Trutnevyte, E., Muntendam-Bos,  
 1466 A., & Wiemer, S. (2024). Managing induced seismicity risks from enhanced geothermal  
 1467 systems: A good practice guideline. *Reviews of Geophysics*,  
 1468 <https://doi.org/10.1029/2024RG000849>.



- 1469  
1470 Zhuang, L., Kim, K. Y., Jung, S. G., Diaz, M., Min, K. B., Zang, A., ... & Hofmann, H.  
1471 (2019). Cyclic hydraulic fracturing of pocheon granite cores and its impact on breakdown  
1472 pressure, acoustic emission amplitudes and injectivity. *International Journal of Rock*  
1473 *Mechanics and Mining Sciences*, 122, 104065, <https://doi.org/10.1016/j.ijrmms.2019.104065>.  
1474  
1475 Zimmermann, G., Zang, A., Stephansson, O., Klee, G., & Semiková, H. (2019). Permeability  
1476 enhancement and fracture development of hydraulic in situ experiments in the Äspö Hard  
1477 Rock Laboratory, Sweden. *Rock Mechanics and Rock Engineering*, 52, 495-515,  
1478 <https://doi.org/10.1007/s00603-018-1499-9>.  
1479  
1480 Zöller, G., & Holschneider, M. (2016). The earthquake history in a fault zone tells us almost  
1481 nothing about Mmax. *Seismological Research Letters*, 87(1), 132-137,  
1482 <https://doi.org/10.1785/0220150176>.  
1483  
1484